Progress In Electromagnetics Research B, Vol. 65, 81–108, 2016

Optimized Superconducting Nanowire Single Photon Detectors to Maximize Absorptance

Mária Csete[1, *], Gábor Szekeres[1], András Szenes[1], Balázs Bánhelyi[2], Tibor Csendes[2], and Gábor Szabó[1]

Abstract—Dispersion characteristics of four types of superconducting nanowire single photon detectors, nano-cavity-array-(NCA-), nano-cavity-deflector-array-(NCDA-), nano-cavity-double-deflector-array-(NCDDA-) and nano-cavity-trench-array-(NCTA-) integrated (A-SNSPD) devices were optimized in three periodicity intervals commensurate with half-, three-quarter- and one surface plasmon polariton wavelength. The optimal configurations capable of maximizing absorptance in niobium nitride correspond to periodicity-dependent tilting in S-orientation (90° azimuthal orientation). In NCAI-A-SNSPDs absorptance maxima are reached at the plasmonic Brewster angle due to light tunneling. The absorptance maximum is attained in a wide plasmonic-pass-band in $NCDAI_{1/2*\lambda}$-A, inside a flat-plasmonic-pass-band in $NCDAI_{3/4*\lambda}$-A and inside a narrower plasmonic-band in $NCDAI_{\lambda}$-A. In $NCDDAI_{1/2*\lambda}$-A bands of strongly-coupled cavity and propagating plasmonic modes cross, in $NCDDAI_{3/4*\lambda}$-A an inverted-plasmonic-band-gap develops, while in $NCDDAI_{\lambda}$-A a narrow plasmonic-pass-band appears inside an inverted-minigap. The absorptance maximum is achieved in $NCTAI_{1/2*\lambda}$-A inside a plasmonic-pass-band, in $NCTAI_{3/4*\lambda}$-A at an inverted-plasmonic-band-gap center, while in $NCTAI_{\lambda}$-A inside an inverted-minigap. The highest 95.05% absorptance is attained at perpendicular incidence onto $NCTAI_{\lambda}$-A. Quarter-wavelength type cavity modes contribute to the near-field enhancement around NbN segments except in $NCDAI_{\lambda}$-A and $NCDDAI_{3/4*\lambda}$-A. The polarization contrast is moderate in NCAI-A-SNSPDs ($\sim 10^2$). NCDAI- and NCDDAI-A-SNSPDs make possible to attain considerably large polarization contrast ($\sim 10^2 - 10^3$ and $\sim 10^3 - 10^4$), while NCTAI-A-SNSPDs exhibit a weak polarization selectivity ($\sim 10 - 10^2$).

1. INTRODUCTION

Single-photon generation and detection are key steps of quantum information processing (QIP) [1–8]. The main characteristic parameters of single-photon detectors include detection efficiency, dark-count rate, reset time and timing jitter. Superconducting materials are widely used in single-photon detectors, e.g., in superconducting nanowire single-photon detectors (SNSPD) [1–33]. The physical mechanism of absorptance in SNSPDs includes the hot spot formation in the superconducting segments caused by infrared photon incidence. The system detection efficiency of SNSPDs is determined as $SDE = \eta * A * P$, where η qualifies the efficiency of coupling from free space. A is the absorptance determined by geometrical and optical properties of the absorbing segments, and P indicates the probability that the incident photon generates a voltage signal. There are several efforts described in the literature to improve SNSPDs performance by tailoring the superconducting pattern properties. The P registering probability was enhanced via ultra-narrow superconducting niobium nitride (NbN) wires [22] and by applying novel superconducting materials [19, 28, 29].

Received 9 September 2015, Accepted 24 November 2015, Scheduled 7 January 2016
* Corresponding author: Maria Csete (mcsete@physx.u-szeged.hu).
[1] Department of Optics and Quantum Electronics, University of Szeged, Dóm tér 9, Szeged, H-6720, Hungary. [2] Institute of Informatics, University of Szeged, Árpád tér 2, Szeged, H-6720, Hungary.

It was shown that meandered superconducting patterns with rounded corners make it possible to enhance the critical current and to reduce dark current [27].

According to Ginzberg-Landau theory, shorter nanowires possess smaller kinetic inductance causing shorter reset time [9]; therefore, various nanophotonical methodologies were developed to enhance the absorptance via short meandered superconducting patterns. Nano-cavities have been primarily applied to enhance the $\eta_{cavity} * A$ effective absorption cross-section in $SDE = \eta_{external} * \eta_{cavity} * A * P$ detection efficiency, where $\eta_{external}$ refers to the probability that a single-photon enters the nanophotonically modified environment [10, 13, 18, 19, 23, 25]. Distributed Bragg reflectors and multi-layers acting as optical cavities were also implemented [21, 29]. Plasmonic structures capable of improving light-in-coupling via localized and propagating modes were recently integrated into SNSPDs, and enhanced effective absorption cross-section was achieved qualified by $\eta_{plasmonic} * A$ quantity in $SDE = \eta_{external} * \eta_{plasmonic} * A * P$ [24, 26, 31–33]. Moreover, it was shown that the plasmonic nature of superconducting stripes can also be used to realize efficient single-photon detection [30].

Superconducting NbN stripes embedded into dielectric media and into optical cavities inherently prefer **E**-field oscillation parallel to their long axes [13, 23, 25]. To quench the corresponding polarization sensitivity of detectors, a spiral geometry was proposed [14], and two mutually perpendicular patterns were stacked vertically into a multilayer cavity [28]. The polarization sensitivity of superconducting patterns located in close proximity of antennas and embedded into complex plasmonic structures differs fundamentally from that of bare stripes [24, 26, 31–33]. Superconducting NbN patterns integrated with 1D periodic plasmonic structures of different types exhibit enhanced absorptance at azimuthal orientations corresponding to the **E**-field oscillation perpendicular to noble metal segments [26, 31, 33]. Based on our previous results, the *p*-polarized absorptance can be significantly improved with respect to the *s*-polarized one; therefore, plasmonic structure integrated devices are particularly promising in QIP applications, where polarization selectivity is very important, e.g., in Bennett and Bassard QKD protocol (BB84) [26, 31, 33–35]. Detector designs ensuring QI specific read-out are crucial to avoiding different attack schemes and in the development of optical quantum computers [7, 8, 36, 37].

All previous examples in the literature about SNSPD improvement are based on preconceptions regarding the structure parameters that are capable of enhancing detection efficiency. However, complete numerical optimization of integrated device structures has not been realized until now. The main purpose of our present work was to determine those configurations of four different types of plasmonic structure integrated SNSPDs capable of maximizing the absorptance at 1550 nm wavelength, as well as to analyze the polarization contrast, which can be achieved via these A-SNSPD type devices. In addition, we have analyzed tendencies in configurations of four corresponding C-SNSPD type devices, which make possible to maximize the polarization contrast by gradually decreasing the criterion regarding the absorptance that have to be met parallel. These results are presented in Appendix A. (Figures A1–A4).

2. METHODS

Four different types of plasmonic structure integrated SNSPDs were inspected theoretically, and for each design type, three periodicity regions were considered, where special nanophotonical phenomena are at play (Figures 1, 2). Taking into account the λ_{SPP} wavelength of the surface plasmon polaritons (SPPs) excitable at silica substrate and gold interface at 1550 nm, periodicity regions commensurate with $0.5*\lambda_{SPP}/0.75*\lambda_{SPP}/\lambda_{SPP}$ were considered, where Bragg scattering/extraordinary transmission/Rayleigh phenomena are expected.

In nano-cavity-array integrated NCAI-A-SNSPDs each niobium nitride (NbN) stripe is surrounded by vertical gold segments composing a metal-insulator-metal (MIM) nano-cavity-grating (Figures 1(a), 2(a)) [26, 31, 33]. In nano-cavity-deflector-array integrated NCDAI-A-SNSPDs additional gold segments nominated as deflectors are inserted into the silica substrate at the anterior sides of each NbN loaded nano-cavity (Figures 1(b), 2(b)) [31, 33]. In nano-cavity-double-deflector-array integrated NCDDAI-A-SNSPDs, both at their anterior and exterior sides, each nano-cavity is neighbored by gold deflectors, which can have different lengths and widths (Figures 1(c), 2(c)) [33]. In contrast, in nano-cavity-trench-array integrated NCTAI-A-SNSPDs trenches are embedded into the in-plane interleaved vertical gold segments, which can have different widths (Figures 1(d), 2(d)) [33, 38]. Insertion of trenches, which are also capable of acting as efficient plasmonic mirrors, makes it possible to reduce the total amount of

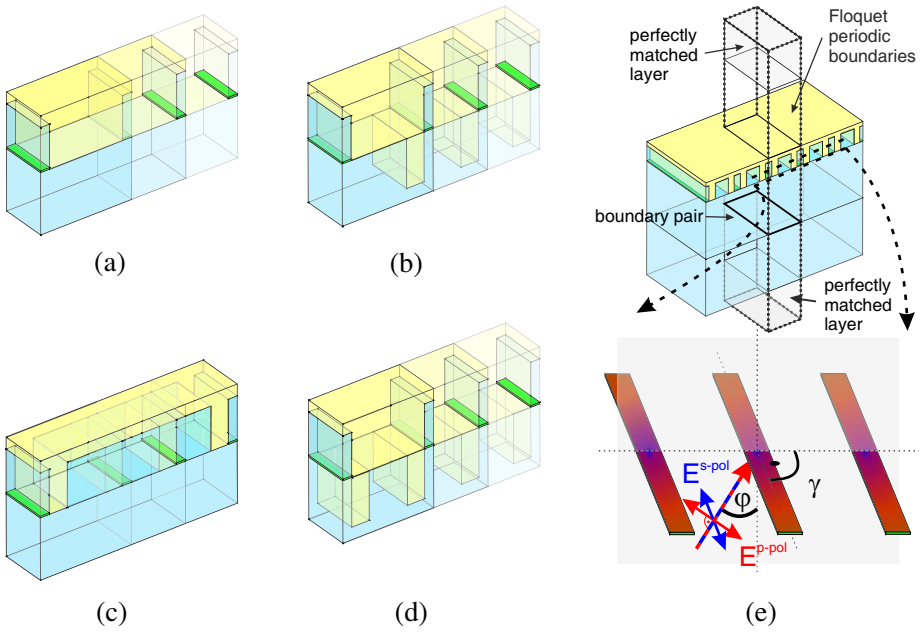

Figure 1. Three dimensional view of inspected (a) NCAI-, (b) NCDAI-, (c) NCDDAI- and (d) NCTAI-A-SNSPD with three different periods. (e) Illumination methodology indicating one unit cell of an infinite pattern between Floquet periodic boundary conditions vertically. Inset: polar angle (φ), azimuthal orientation (γ), and **E**-field oscillation direction in p- and s-polarized light indicated on the magnified view of absorbing superconducting NbN segments heated by p- and s-polarized light.

gold, which causes a competitive absorption.

Theoretical studies were performed to determine the optimal configurations for each type of SNSPD designs, using the special finite element method that we have previously developed based on the Radio Frequency module of COMSOL Multiphysics software package (COMSOL AB) [23, 25, 26, 31, 33]. The index of refraction of dielectric materials (silica, $NbNO_x$ and HSQ) was specified via Cauchy formulae, while dielectric constants for both absorbing materials (NbN, Au) were loaded from tabulated datasets.

We have applied an in-house developed efficient optimization technique, nominated as GLOBAL, for the solution of all problems emerging during SNSPD optimization, which was implemented using LiveLink for MATLAB in COMSOL. GLOBAL is a stochastic technique that is a sophisticated composition of sampling, clustering, and local search [39]. GLOBAL was also used successfully for the solution of very complex optimization problems, such as the mathematical proof of the chaotic behavior of the forced damped pendulum [40] and for proving a long standing conjecture of Wright on delay differential equations [41].

Three-dimensional models were used to determine the optimal structure and the corresponding optimal illumination direction, which are capable of resulting in maximal absorptance, i.e., the optimal configuration of A-SNSPD type devices (Figure 1(e)). The absorptance in the superconducting NbN (as well in gold) is determined based on the resistive heating ($Q^{p\text{-}pol/s\text{-}pol}$) inside the corresponding segments, which is normalized by the entire power of the incoming light (P_{in}): $A^{p\text{-}pol/s\text{-}pol} = Q^{p\text{-}pol/s\text{-}pol}/P_{in}$, as described in our previous work [23]. All geometrical parameters and the φ polar angle were varied at fixed $\gamma = 90^\circ$ azimuthal angle (nominated as S-orientation), which results in the largest achievable absorptance in case of different plasmonic structure integrated SNSPDs, based on our previous studies (Figure 1(e), inset) [26, 31, 33].

The dispersion characteristics in NbN absorptance were determined in the optimal S-orientation of four integrated A-SNSPD device types for three periodicity intervals as well and are presented in Figure 3. The angle-dependent absorptance of the optimized SNSPDs was analyzed first for 1550 nm p-polarized light illumination, then the wavelength dependency at the absorptance maxima was also inspected to uncover the underlying nanophotonical phenomena (Figure 3 and Figure 5).

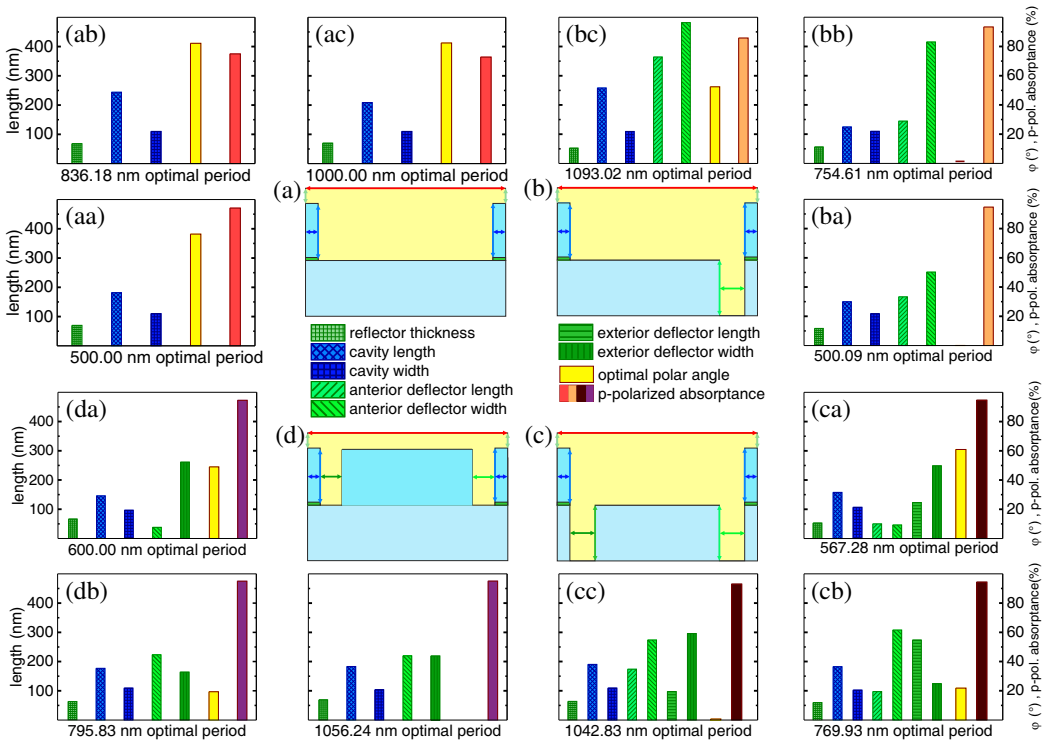

Figure 2. Schematics of geometry optimization method of (a) NCAI-, (b) NCDAI-, (c) NCDDAI- and (d) NCTAI-A-SNSPD. Histograms showing the optimized geometrical parameters, p-polarized absorptance and optimal polar angle in (aa) $NCAI_{1/2*\lambda}$-, (ab) $NCAI_{3/4*\lambda}$-, (ac) $NCAI_{\lambda}$-, (ba) $NCDAI_{1/2*\lambda}$-, (bb) $NCDAI_{3/4*\lambda}$-, (bc) $NCDAI_{\lambda}$-, (ca) $NCDDAI_{1/2*\lambda}$-, (cb) $NCDDAI_{3/4*\lambda}$-, (cc) $NCDDAI_{\lambda}$-, (da) $NCTAI_{1/2*\lambda}$-, (db) $NCTAI_{3/4*\lambda}$- and (dc) $NCTAI_{\lambda}$-A-SNSPD.

The time-averaged **E**-field distribution was studied along with the power-flow at the maxima in polar angle on the NbN absorptance, at plane cross-sections taken perpendicular to single unit cells of the integrated SNSPDs (Figures 1(a)–(d), 2(a)–(d), 4). The **E**-field time-evolution was inspected as well to characterize all localized and propagating modes supported by the integrated periodic patterns (see Multimedia files 1–12). We have inspected the polarization contrast (PC) in S-orientation, namely the ratio of absorptances achievable via p- and s-polarized light illumination, which equals the ratio of the resulted Joule-heating: $PC = A^{p\text{-}pol}/A^{s\text{-}pol} = Q^{p\text{-}pol}/Q^{s\text{-}pol}$. The polar-angle and wavelength-dependent polarization contrast was also analyzed for integrated A-SNSPD type devices (Figure 5).

3. RESULTS

The optimization results indicated that the optimal configurations were device design specific, and the detailed inspection of the optimized A-SNSPD type devices' dispersion characteristics and near-field distribution revealed that the underlying nanophotonics fundamentally depended on the integrated structure type and on the periodicity interval.

3.1. Parameters and Dispersion Characteristics of Optimized A-SNSPD Configurations

The optimization of half-wavelength-scaled integrated $NCAI_{1/2*\lambda}$-A-SNSPD pattern resulted in 500 nm optimal pitch and 110 nm optimal MIM nano-cavity width, which corresponded to the lower and upper bounds of the inspected periodicity and nano-cavity width interval, respectively (Figure 2(aa)).

This suggests that allowing smaller periodicities will result in even higher absorptance, however, at

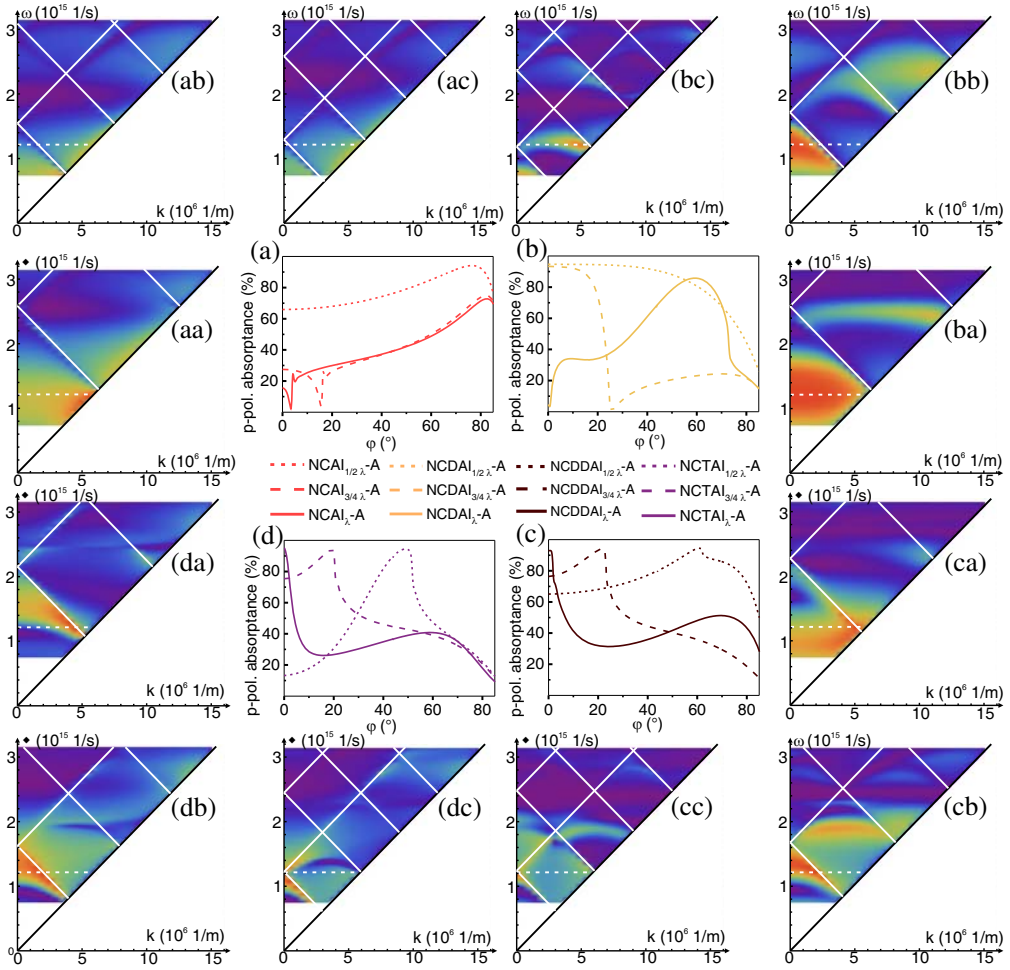

Figure 3. Polar-angle-dependent p-polarized absorptances at 1550 nm of (a) NCAI-, (b) NCDAI-, (c) NCDDAI- and (d) NCTAI-A-SNSPD at $\gamma = 90°$ azimuthal orientation (in S-orientation). Dispersion diagrams of (aa) $NCAI_{1/2*\lambda}$-, (ab) $NCAI_{3/4*\lambda}$-, (ac) $NCAI_{\lambda}$-, (ba) $NCDAI_{1/2*\lambda}$-, (bb) $NCDAI_{3/4*\lambda}$-, (bc) $NCDAI_{\lambda}$-, (ca) $NCDDAI_{1/2*\lambda}$-, (cb) $NCDDAI_{3/4*\lambda}$-, (cc) $NCDDAI_{\lambda}$-, (da) $NCTAI_{1/2*\lambda}$-, (db) $NCTAI_{3/4*\lambda}$- and (dc) $NCTAI_{\lambda}$-A-SNSPD in S-orientation.

the expense of kinetic inductance and reset time increase. Therefore, we have finalized the optimization procedure at this pitch. The nano-cavity length is 181.44 nm in the optimized $NCAI_{1/2*\lambda}$-A device (Figure 2(aa)).

The dispersion diagram of the optimized $NCAI_{1/2*\lambda}$-A shows that the absorptance is enhanced throughout almost the entire polar angle interval in a wide spectral region around 1550 nm (Figure 3(aa)). Moreover, the NbN absorptance is locally enhanced at tilting corresponding to the wavelength-dependent plasmonic Brewster angle (PBA) close to the first Brillouin zone boundary [31, 33, 42–44]. The collective resonance on the half-wavelength-scaled nano-cavity-array results in slightly polar-angle-dependent absorptance (Figure 3(a)), according to previous observations on short-pitch gratings [45–48]. Namely, the absorptance is 65.97% already at perpendicular incidence and increases monotonically through large angles. The 94.18% global maximum is attained at 76.38° tilting, which corresponds to the PBA of the $NCAI_{1/2*\lambda}$-A.

The optimization of three-quarter-wavelength-scaled $NCAI_{3/4*\lambda}$-A-SNSPD integrated device resulted in 836.18 nm optimal periodicity. The 109.97 nm nano-cavity width is almost equal to corresponding optimal width of $NCAI_{1/2*\lambda}$-A, while the 243.79 nm nano-cavity length is significantly larger (Figure 2(ab)). The dispersion graph of the optimized $NCAI_{3/4*\lambda}$-A device shows that

considerably smaller absorptance is attainable, inside a significantly smaller polar angle and wavelength interval (Figure 3(ab)). In addition to this, the $NCAI_{3/4*\lambda}$-A is capable of coupling the incident light into surface waves at small tilting, which causes a significant modulation on the dispersion curve [49–53]. The absorptance maxima appear close to the second Brillouin zone boundary. At 1550 nm the light in-coupling results in a 3.75% global absorptance minimum at 15.60° polar angle (Figure 3(a)), which is followed by a local absorptance maximum-minimum pair resulting in 27.35% and 21.82% absorptance at 16.50° and 17.30° tilting, respectively. These features are in accordance with Wood-anomaly [31, 33, 53–56]. By increasing the polar angle, a monotonic NbN absorptance increase is observable through the PBA [31, 33, 42–44]. The light tunneling phenomena result in a global absorptance maximum of 74.96% at 82.24° tilting.

The optimization of wavelength-scaled $NCAI_{\lambda}$-A-SNSPD resulted in maximal NbN absorptance in 1000 nm pitch pattern of 110 nm width MIM nano-cavities, which corresponds to the lower and upper bounds of periodicity and cavity width intervals, respectively (Figure 2(ac)). The highest absorptance is achieved via nano-cavities with intermediate 208.82 nm optimal length. The dispersion characteristics are similar to that of $NCAI_{3/4*\lambda}$-A and exhibit a grating coupling related modulation [49–53]. The absorptance modulation caused by coupling to surface modes appears at smaller polar angles according to the increased periodicity (Figure 3(ac)) [31, 33, 53–56]. The largest absorptance is achieved close to the second Brillouin zone boundary. At 1550 nm 2.15% global minimum appears at 3.40° tilting, which is followed by a local maximum-minimum pair, manifesting itself in 24.51% and 19.63% NbN absorptance at 4.2° and 5.1° tilting. Then the NbN absorptance monotonously increases through the 72.82% global absorptance maximum appearing at 82.46° tilting corresponding to the PBA (Figure 3(a)) [31, 33, 42–44]. The attained absorptance is smaller than the absorptance observed in either of the $NCAI_{1/2*\lambda}$-A and $NCAI_{3/4*\lambda}$-A devices almost in the entire polar angle interval.

The optimization of half-wavelength-scaled $NCDAI_{1/2*\lambda}$-A-SNSPD resulted in 500.09 nm optimal periodicity and 108.72 nm optimal nano-cavity width (Figure 2(ba)). Their noticeable difference with respect to lower/upper optimization bounds proves that the parameters correspond to an efficiently optimized design. The 149.89 nm nano-cavity length in the optimized device is even smaller than in the case of $NCAI_{1/2*\lambda}$-A. The optimized 166.46 nm length of deflectors is slightly larger, and in spite of their large 250.98 nm width, large NbN absorptance is attained. The dispersion diagram of the optimized $NCDAI_{1/2*\lambda}$-A shows that this integrated device supports collective resonance in a plasmonic pass band covering the widest spectral and polar angle interval, and almost polar-angle-independent absorptance is achieved according to the sub-wavelength pitch (Figure 3(ba)) [45–48]. The absorptance maxima appear close to perpendicular incidence in a wide spectral region, then the absorptance decreases monotonously towards the first Brillouin zone boundary. The slightly polar-angle-dependent absorptance of $NCDAI_{1/2*\lambda}$-A shows a 94.68% global maximum close to perpendicular incidence at 0.04° tilting. The absorptance decreases monotonically also at 1550 nm revealing the absence of PBA corresponding to NbN loaded nano-cavity-array.

The optimization of three-quarter-wavelength-scaled integrated $NCDAI_{3/4*\lambda}$-A-SNSPD device resulted in 754.62 nm periodicity close to the lower bound. The 109.61 nm nano-cavity width is slightly larger than in $NCDAI_{1/2*\lambda}$-A. The 124.49 nm and 144.55 nm nano-cavity and deflector lengths are slightly smaller but commensurate with those in $NCDAI_{1/2*\lambda}$-A. In contrast to intuitive expectations, the 415.24 nm optimized deflector width is considerably larger than the width of deflectors in $NCDAI_{1/2*\lambda}$-A (Figure 2(bb)). The dispersion graph of the optimized $NCDAI_{3/4*\lambda}$-A device shows that in the presence of deflectors, large absorptance is achieved through a significant fraction of the first Brillouin zone. The largest absorptance is attainable already at perpendicular incidence in wide spectral interval inside a flat plasmonic pass band, which is noticeably smaller than in $NCDAI_{1/2*\lambda}$-A (Figure 3(bb)). The $NCDAI_{3/4*\lambda}$-A is capable of coupling the incident light into surface waves at regions of small transitional tilting with large efficiency. The flat pass-band on the dispersion curve is followed by a well-defined cut-off, where the first order grating coupling occurs [49–53]. The absorptance of $NCDAI_{3/4*\lambda}$-A is 93.34% at perpendicular incidence (Figure 3(b)), which is the global maximum of this device. The absorptance decreases by increasing the polar angle, at 25.50° polar angle reaches 0.76%, i.e., it is almost zero according to the cut-off on the integrated structure. This orientation corresponds to the first Brillouin zone boundary, where the integrated pattern couples in -1 order into backward propagating Brewster-Zenneck modes in the composite diffracted field. These modes have a 1084.42 nm wavelength, which

is larger than the photonic wavelength [49–53, 57–60]. For larger polar angles, the NbN absorptance increases slowly again. However, only a weak absorptance enhancement is observable in the region, where PBA phenomenon originating from array of NbN loaded cavities is expected.

The optimization of wavelength-scaled NCDAI$_\lambda$-A-SNSPD resulted in the largest absorptance in 1093.02 nm pitch integrated pattern consisting of 109.41 nm wide nano-cavities, whose parameters are closer to the upper bound (Figure 2(bc)). The 258.02 nm nano-cavity length is considerably larger than in corresponding NCDAI$_{1/2*\lambda}$-A and NCDAI$_{3/4*\lambda}$-A devices. The deflectors having 364.02 nm length and 481.46 nm width are the longest and widest among all optimized SNSPD devices. The dispersion characteristics significantly differ from that of the NCDAI$_{1/2*\lambda}$-A and NCAI$_{3/4*\lambda}$-A devices and indicate a weaker and narrower plasmonic band (Figure 3(bc)) [49–53]. The largest NbN absorptance is achieved close to the second Brillouin zone boundary due to grating coupling in -2 order into backward propagating modes. The absorptance characteristics of NCDAI$_\lambda$-A at 1550 nm significantly differ from that of two other NCDAI-A-SNSPD devices. Namely, the NbN absorptance is 4.5% at perpendicular incidence, then increases rapidly until 5.00° polar angle, and after an inflection point further significant increase is observable. The 85.77% global absorption maximum appears at 59.25° tilting, whose polar angle is significantly smaller than the PBA corresponding to the array of NbN loaded nano-cavities. The 1093.02 nm pitch grating couples in -2 order at this tilting into surface modes having a 975.45 nm wavelength, which is significantly smaller than the photonic wavelength, and indicates cavity and propagating modes' interaction [26, 31, 33, 49, 50]. The attained absorptance is smaller than in NCDAI$_{3/4*\lambda}$-A through $\sim$ 25.00° polar angle, while it is overridden by the absorptance achieved in NCDAI$_{1/2*\lambda}$-A almost throughout the entire polar angle interval.

The optimization of half-wavelength-scaled NCDDAI$_{1/2*\lambda}$-A-SNSPD resulted in 567.82 nm optimal periodicity and 106.77 nm nano-cavity width, which are close to the upper bounds (Figure 2(ca)). The 157.69 nm nano-cavity length is intermediate compared to those of NCAI$_{1/2*\lambda}$-A and NCDAI$_{1/2*\lambda}$-A. The 50 nm/123.26 nm lengths and 46.36 nm/248.79 nm widths reveal that gold deflectors at the anterior/exterior side of nano-cavities play negligible/dominant role (see Appendix Figure A3(ca)). According to the dispersion diagram of NCDDAI$_{1/2*\lambda}$-A, the desired 1550 nm is at the upper edge of a strongly-coupled region of a collectively resonant nano-cavity mode and a backward propagating surface mode originating from -1 order grating coupling (Figure 3(ca)) [50, 62]. The strong-coupling phenomenon results in local enhancement inside a characteristic cross-shaped area proving mode-hybridization. The absorptance is slightly polar-angle-dependent in NCDDAI$_{1/2*\lambda}$-A according to collective resonances on the sub-wavelength nano-cavity-array [45–48]. The NbN absorptance is 65.00% at perpendicular incidence and monotonically increases with tilting until a modulation, which results in a 94.60% global absorptance maximum at 60.89°. The 1060.19 nm wavelength of the backward propagating modes coupled in -1 order indicates their plasmonic nature [31, 33]. The absorptance decreases monotonously towards the first Brillouin zone boundary indicating that light tunneling phenomenon at the PBA originating from array of NbN loaded nano-cavities is depressed also in the presence of double deflectors.

The optimization of three-quarter-wavelength scaled NCDDAI$_{3/4*\lambda}$-A-SNSPD resulted in 769.93 nm periodicity and 102.24 nm nano-cavity width, close to the lower bound (Figure 2(cb)). In NCDDAI$_{3/4*\lambda}$-A, the smaller cavity width is accompanied by larger 182.15 nm length than NCDDAI$_{1/2*\lambda}$-A. The 97.04 nm/273.12 nm ratio of deflector lengths at the anterior/exterior sides is slightly decreased with respect to that observed in NCDDAI$_{1/2*\lambda}$-A, while the ratio of their 307.43 nm/124.13 nm widths is reversed, which reveals that the two gold deflectors play more compensated role (see Figure A3(cb) in Appendix A). The dispersion graph of the optimized NCDDAI$_{3/4*\lambda}$-A device indicates a plasmonic pass band, where large absorptance is attainable at transitional tilting in an intermediate spectral interval (Figure 3(cb)) [49–53]. The NCDDAI$_{3/4*\lambda}$-A is capable of coupling the incident light in -1 order into backward propagating right-phase surface modes at tilting similar to the polar angle corresponding to cut-off in NCDAI$_{3/4*\lambda}$-A. This indicates that double deflectors evolve phase correction effect on the coupled propagating modes [33]. The largest absorption is achieved close to the top of the first Brillouin zone inside an inverted plasmonic band-gap. NCDDAI$_{3/4*\lambda}$-A shows an enhanced 76.39% absorptance already at perpendicular incidence. By increasing tilting the absorptance increases until 21.85° polar angle, where 94.34% global maximum is achieved due to coupling in -1 order into backward propagating surface modes having a wavelength of 1052.13 nm. This wavelength indicates that plasmonic modes are

coupled at the inverted PBG center. By increasing tilting further the absorptance does not indicate enhancement at PBA corresponding to the array of NbN loaded nano-cavities.

The optimization of wavelength-scaled NCDDAI$_\lambda$-A-SNSPD resulted in maximal absorptance in 1042.83 nm pitch integrated pattern consisting of 109.15 nm wide nano-cavities (Figure 2(cc)). Although the optimal 190.06 nm nano-cavity length is again larger than in NCDDAI$_{1/2*\lambda}$-A and NCDDAI$_{3/4*\lambda}$-A, it is smaller than the optimal nano-cavity length in counterpart NCDAI$_\lambda$-A. The deflectors at the anterior/exterior side of the cavities has larger/smaller length than NCDDAI$_{1/2*\lambda}$-A and NCDDAI$_{3/4*\lambda}$-A (see Figure A3(cc) in Appendix A). The large 173.89 nm/97.32 nm lengths and 273.48 nm/295.77 nm widths at the anterior/exterior sides result in large competitive gold volume fraction. The dispersion characteristics indicate that not only the achieved absorptance, but also the extension of corresponding frequency-polar angle region is the smallest in NCDDAI$_\lambda$-A (Figure 3(cc)). The peculiarity of this device is that both forward and backward coupled modes contribute to the NbN absorptance maximum. The absorptance maxima are attained inside a narrow plasmonic pass band, which originates from inversion of the plasmonic minigap at the top of the first Brillouin zone [49]. The absorptance characteristics of NCDDAI$_\lambda$-A at 1550 nm resemble the inversion of that in NCDAI$_\lambda$-A at small tilting. In NCDDAI$_\lambda$-A, the 93.00% global absorptance maximum appears near perpendicular incidence at 0.69°. The wavelength-scaled pattern couples in $+/-1$ order into forward and backward propagating modes with slightly different 1030.75 nm and 1055.2 nm wavelengths, respectively. The wavelengths of both coupled modes indicate their plasmonic nature. The absorptance decreases rapidly, then reaches a 51.24% local maximum at 69.5°, which is significantly smaller than the PBA originating from array of NbN loaded nano-cavities.

The optimization of half-wavelength-scaled NCTAI$_{1/2*\lambda}$-A-SNSPD resulted in 600.00 nm optimal periodicity and 96.50 nm nano-cavity width, and 145.81 nm nano-cavity length (Figure 2(da)). The small 38.10 nm and 260.83 nm widths of vertical gold segments neighboring the MIM nano-cavities at their anterior/exterior side make possible to reach very large absorptance in spite of the narrow absorbing NbN stripes (see Figure A4(ca) in Appendix A). The dispersion diagram of NCTAI$_{1/2*\lambda}$-A indicates that the inspected 1550 nm is inside a plasmonic pass band originating from backward propagating surface modes coupled in -1 order (Figure 3(da)) [49–53]. However, the absorptance enhancement is more strongly tilting-dependent than NCDDAI$_{1/2*\lambda}$-A and is significant only inside a narrower regime inside the first Brillouin zone in spite of the sub-wavelength pitch [45–48]. This indicates that NCTAI$_{1/2*\lambda}$-A devices can be used efficiently under optimized illumination conditions. The course of absorptance in NCTAI$_{1/2*\lambda}$-A resembles the NCDDAI$_{1/2*\lambda}$-A, however exhibits a more pronounced polar-angle dependence. Namely, the absorptance is 13.25% at perpendicular incidence and increases rapidly with the polar angle until 49.00°, where it reaches the 94.49% global absorptance maximum. At this orientation, the integrated plasmonic pattern couples into backward propagating surface modes in -1 order. Their short 1041.51 nm wavelength indicates that these are plasmonic modes. The fingerprint of the PBA corresponding to array of NbN loaded nano-cavities is not observable.

The optimization of three-quarter-wavelength-scaled NCTAI$_{3/4*\lambda}$-A-SNSPD resulted in 795.83 nm periodicity at the middle of the optimization interval, and 109.18 nm nano-cavity width close to the upper bound (Figure 2(db)). Both the cavity width and accompanying 176.78 nm length are commensurate with those in NCDDAI$_{3/4*\lambda}$-A, and their ratio is similarly increased with respect to NCTAI$_{1/2*\lambda}$-A. The 222.98 nm and 163.96 nm widths of vertical gold segments at anterior and exterior sides of MIM nano-cavities are more commensurate, while their ratio is reversal with respect to those in NCTAI$_{1/2*\lambda}$-A (see Figure A4(cb) in Appendix A). The dispersion graph of the optimized NCTAI$_{3/4*\lambda}$-A device indicates again a plasmonic pass band [49–53], where the global absorptance maximum is achieved at transitional tilting in a wider spectral interval compared to NCTAI$_{1/2*\lambda}$-A (Figure 3(db)). The NCTAI$_{3/4*\lambda}$-A more efficiently couples the incident light in -1 order into backward propagating right-phase surface modes. As a result, larger absorption is achieved inside an inverted plasmonic band-gap at the top of the first Brillouin zone. The NCTAI$_{3/4*\lambda}$-A devices absorptance characteristics are similar to the corresponding NCDDAI$_{3/4*\lambda}$-A; however, all absorptance values are slightly larger, and the extrema are shifted to smaller polar angles. The NCTAI$_{3/4*\lambda}$-A device shows 75.37% absorptance already at perpendicular incidence, then by increasing tilting, the absorptance increases until 19.37° polar angle, where 94.95% global maximum is achieved. At this tilting light coupling occurs in -1 order into backward propagating surface modes having a wavelength of 1056.99 nm, which exhibits plasmonic

characteristics. The absorptance decreases monotonously by increasing tilting, i.e., PBA corresponding to array of NbN loaded nano-cavities is not observable.

The optimization of wavelength-scaled NCTAI$_\lambda$-A-SNSPD resulted in the largest absorptance in 1056.24 nm pitch integrated pattern, and this value almost equals the wavelength of plasmons, which propagate at semi-infinite silica-gold interface. The 103.69 nm optimal widths of nano-cavities are the smallest among wavelength-scaled integrated devices (Figure 2(dc)). The optimal 183.2 nm nano-cavity length is larger than the length in corresponding NCTAI$_{1/2*\lambda}$-A and NCTAI$_{3/4*\lambda}$-A devices, and it is decreased with respect to optimal nano-cavity length in NCDDAI$_\lambda$-A. The 219.46 nm and 219.03 nm widths of vertical gold segments at the anterior and exterior sides of the nano-cavities are almost the same (see Appendix Figure A4(cc)). Among NCTAI-A devices, the dispersion characteristics of NCTAI$_\lambda$-A indicate the smallest extension of frequency-polar angle region, where significant absorptance enhancement occurs (Figure 3(dc)). Both forward and backward coupled modes contribute to the absorptance maximum at the zones crossing point. The largest absorptance is attained inside an inverted plasmonic minigap at the top of the first Brillouin zone similar to NCDDAI$_\lambda$-A [49]; however, the achieved absorptance is larger. The absorptance characteristics of NCTAI$_\lambda$-A at 1550 nm are very similar to that of NCDDAI$_\lambda$-A. Most important result of this work is that NCTAI$_\lambda$-A shows the highest achievable NbN absorptance among all inspected SNSPD devices, namely 95.05% absorptance is achieved at perpendicular incidence. The wavelength-scaled pattern couples into forward and backward propagating modes in 1 and -1 order with the same 1056.24 nm wavelength, which refers to SPPs propagating at the gold-substrate interface. The polar-angle-dependent absorptance decreases first dramatically, then reaches a 40.82% local maximum at 58.8°, which is smaller than the PBA corresponding to NbN loaded nano-cavities.

3.2. Role of Near-Field Distribution and Volume-Fraction-Ratio of Absorbing Segments

The limits in achievable absorptance can be understood by comparing the **E**-field time-evolution in optimized devices and the volume-fraction-ratio of absorbing materials (Multimedia files 1–12, see Figures A1(c), A2(c), A3(c) and A4(c) in Appendix A). The distribution of the time-averaged near-field at the maxima in each optimized NCAI-SNSPD type device confirms that the **E**-field is strongly enhanced at the entrance of NbN loaded MIM nano-cavities with $\sim < (\lambda/4)$ length at tilting corresponding to PBA, and the reflected waves intensity is negligible (Figure 4(aa)–(ac), see Multimedia files 1–3). The **E**-field enhancement is strengthened by light tunneling through the MIM nano-cavities according to the PBA related nanophotonical phenomena [42–44]. The Poynting vector is almost parallel to the interface of the substrate and integrated structure at close proximity of the gold segments while it points to the cavities at their entrance.

In NCAI$_{1/2*\lambda}$-A, the $0.71*(\lambda/4)$ nano-cavity length corresponds to strongly squeezed resonant MIM modes (see Figure 4(aa) and Figure A1(ba) in Appendix A). The time-evolution shows that the **E**-field is highly enhanced in at least one of the neighboring MIM cavities, and both are shined efficiently in significant part of each duty-cycle (see Multimedia file 1). Among NCAI-A-SNSPD devices, the optimized NCAI$_{1/2*\lambda}$-A possess the largest $4.07*10^{-3}$ NbN/Au volume-fraction-ratio (see Figure A1(ca) in Appendix A). In the optimized NCAI$_{3/4*\lambda}$-A, the longer $0.95*(\lambda/4)$ cavity reveals that the resonant MIM modes are less squeezed than in NCAI$_{1/2*\lambda}$-A, but are still capable of ensuring **E**-field enhancement at the entrance of nano-cavities (see Figure 4(ab) and Figure A1(bb) in Appendix A). Although the neighboring cavities are still shined alternately, a significant part of illuminating beam overlaps with the inserted gold segments (see Multimedia file 2). The optimized NCAI$_{3/4*\lambda}$-A exhibits intermediate $1.85*10^{-3}$ NbN/Au volume-fraction-ratio (see Figure A1(cb) in Appendix A). In NCAI$_\lambda$-A, the nano-cavity length commensurate with $0.81*(\lambda/4)$ reveals that the resonant MIM modes are squeezed at medium level (see Figure 4(ac) and Figure A1(bc) in Appendix A). However, a completely distinct **E**-field time evolution is observable in neighboring cavities (see Multimedia file 3). Because of the largest periodicity, the illumination of MIM cavities occurs in the smallest fraction of each duty-cycle, while considerable enhancement is observable below the inserted gold segments as well. This explains that the NbN absorptance is smaller than in the two pervious devices, in spite of the largest **E**-field enhancement at the MIM nano-cavity entrances. The absorptance improving effect is the least efficient in the NCAI$_\lambda$-A device among NCAI-A-SNSPDs, according to the smallest $1.68*10^{-3}$ NbN/Au volume-fraction-ratio (see Figure A1(cc) in Appendix A).

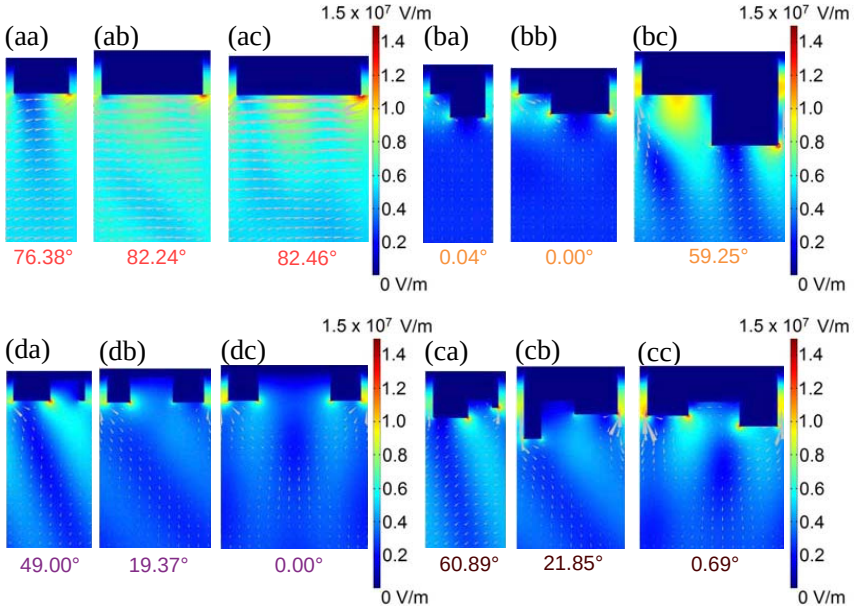

Figure 4. Time-averaged **E**-field and power flow at absorptance maxima in polar angle in optimized (aa) $NCAI_{1/2*\lambda}$-, (ab) $NCAI_{3/4*\lambda}$-, (ac) $NCAI_{\lambda}$-, (ba) $NCDAI_{1/2*\lambda}$-, (bb) $NCDAI_{3/4*\lambda}$-, (bc) $NCDAI_{\lambda}$-, (ca) $NCDDAI_{1/2*\lambda}$-, (cb) $NCDDAI_{3/4*\lambda}$-, (cc) $NCDDAI_{\lambda}$-, (da) $NCTAI_{1/2*\lambda}$-, (db) $NCTAI_{3/4*\lambda}$- and (dc) $NCTAI_{\lambda}$-A-SNSPD.

In optimized $NCDAI_{1/2*\lambda}$-A, the cavity closed by NbN is commensurate with $0.59*(\lambda/4)$, while the $1.22*(\lambda/4)$ extended cavity length is commensurate with, but slightly larger than quarter-wavelength; as a result, it can support $(\lambda/4)$-type resonant MIM modes (see Figure A2(ba) in Appendix A). The time-averaged near-field reveals that the **E**-field is significantly enhanced at the entrance of nano-cavities as well as on the deflector corners (Figure 4(ba)). The Poynting vector indicates a backward directed power-flow, proving that the gold deflector array redirects the incident light towards the preceding nano-cavities. The **E**-field time-evolution shows no reflected waves. On the contrary, the deflectors efficiently guide the nearly perpendicularly incident light towards the NbN segments (see Multimedia file 4). The nano-cavity entrances and deflector corners are shined alternately, and the delay introduced by deflectors into the guided wave propagation ensures that one of the neighboring cavities is illuminated throughout dominant part of each duty-cycle. Compared to $NCAI_{1/2*\lambda}$-A, larger absorptance is achievable in spite of smaller $3.29*10^{-3}$ NbN/Au volume-fraction-ratio (see Figure A2(ca) in Appendix A), due to the larger time-averaged local **E**-field enhancement around the NbN segments.

In optimized $NCDAI_{3/4*\lambda}$-A, the length of nano-cavity closed by NbN is commensurate with $0.49*(\lambda/4)$, i.e., it is two-times smaller than those in $NCAI_{3/4*\lambda}$-A. The $1.04*(\lambda/4)$ length of extended cavities is just slightly larger than quarter-wavelength, indicating that they can support $(\lambda/4)$-type resonant MIM modes (see Figure A2(bb) in Appendix A). Both the time-averaged **E**-field and Poynting vector distribution as well as the **E**-field time-evolution are very similar to those in $NCDAI_{1/2*\lambda}$-A (Figure 4(bb)). The **E**-field is strongly and almost synchronously enhanced at the entrance of neighboring nano-cavities, while at the deflector corners the **E**-field enhancement is not symmetrical and is out-of-phase (see Multimedia file 5). Synchronous illumination of neighboring cavities results in that they contribute to the **E**-field enhancement in significant fraction of each duty-cycle. The $2.35*10^{-3}$ NbN/Au volume-fraction-ratio is just slightly reduced compared to $NCDAI_{1/2*\lambda}$-A (see Figure A2(cb) in Appendix A). The competitive gold absorption is compensated via increased periodicity and decreased deflector length, which helps attain relatively high absorptance.

In optimized $NCDAI_{\lambda}$-A, the nano-cavities closed by NbN have $(\lambda/4)$ length, while the $2.38*(\lambda/4)$ length of extended cavities overrides half-wavelength, indicating that they can support $\sim 3*(\lambda/4)$ type resonant MIM modes (see Figure A2(bc) in Appendix A). The **E**-field enhancement is still large

at the entrance of nano-cavities, and the Poynting vector points towards the NbN segments; however, the **E**-field becomes more significant at the cavity-side corner of deflectors and under the inserted gold segment as well (Figure 4(bc)). The **E**-field time-evolution shows that the preceding nano-cavities, inserted gold segments, deflectors and succeeding nano-cavities are illuminated successively by the incident beam (see Multimedia file 6). In addition to this, the backward propagating modes coupled in -2 order on the integrated structure promote efficient illumination through each duty-cycle. Two **E**-field antinodes are observable vertically along the extended cavities and in each period, according to the order of grating couplings at play [47, 48]. However, the $8.89 * 10^{-4}$ NbN/Au volume-fraction-ratio is significantly decreased compared to NCDAI$_{1/2*\lambda}$-A and NCDAI$_{3/4*\lambda}$-A (see Figure A2(cc) in Appendix A). In addition to this, weak reflected waves are also noticeable in the near-field indicating that conversion into bound surface waves is less efficient. Accordingly, the absorptance improving effect of the integrated gold nano-cavity and deflector grating is the least efficient in the NCDAI$_{\lambda}$-A among NCDAI-A-SNSPD devices.

In optimized NCDDAI$_{1/2*\lambda}$-A, the nano-cavity closed by NbN is commensurate with $0.62 * (\lambda/4)$, while the $0.81 * (\lambda/4)/1.09 * (\lambda/4)$ extended cavity length is slightly smaller/larger than quarter-wavelength for the deflector at the anterior/exterior side (see Figure A3(ba) in Appendix A). This indicates that symmetrical $(\lambda/4)$ type resonant MIM modes are supported in case of illumination at either side of extended cavities. The **E**-field is enhanced at the NbN segments and at the corners on the exterior side of both deflectors (Figure 4(ca)). The Poynting vector also indicates a power-flow towards both nano-cavities. In between the two deflectors, both the **E**-field and the power-flow are weak, and the Poynting vector is parallel with the substrate-gold interface and is directed towards the smaller anterior-side deflector. The **E**-field time-evolution shows that the incident light is effectively directed towards the NbN segments by double deflectors (see Multimedia file 7). The double deflectors with different sizes result in efficient, however slightly asynchronous illumination of the MIM nano-cavities acting as $\sim (\lambda/4)$ resonators. Weak backward propagating surface modes, which originate from -1 order grating coupling, are also observable. The $3.08 * 10^{-3}$ NbN/Au volume fraction ratio is slightly smaller than in NCAI$_{1/2*\lambda}$-A and NCDAI$_{1/2*\lambda}$-A (see Appendix Figure A3(ca)). Accordingly, the absorptance maximum is smaller in the presence of double deflectors.

In optimized NCDDAI$_{3/4*\lambda}$-A, the nano-cavity closed by NbN is commensurate with $0.71 * (\lambda/4)$, while the $1.08 * (\lambda/4)/1.75 * (\lambda/4)$ extended cavity lengths indicate that quarter/half-wavelength type resonant MIM modes are supported in case of illumination at the anterior/exterior deflector side (see Appendix Figure A3(bb)). The **E**-field is enhanced around the NbN segments and at the cavity-side corner of those deflectors, which are positioned at the anterior-side of nano-cavities (Figure 4(cb)). No significant **E**-field enhancement is observable below the inserted gold segment. The Poynting vectors indicate right/left directed power-flow towards the NbN segments along deflectors positioned at their anterior/exterior sides. The cavity resonances in $\sim (\lambda/4)$ and $\sim (\lambda/2)$ modes shine the NbN segments in neighboring nano-cavities alternately. The **E**-field time-evolution indicates well defined backward propagating waves originating from -1 order coupling, while very weak reflected waves are observable under the integrated pattern (see Multimedia file 8). The $1.74 * 10^{-3}$ NbN/Au volume fraction ratio is reduced with respect to NCDDAI$_{1/2*\lambda}$-A (see Figure A3(cb) in Appendix A). Accordingly, the achieved maximal absorptance is smaller.

In optimized NCDDAI$_{\lambda}$-A, the length of cavity closed by NbN is commensurate with $0.74 * (\lambda/4)$. Although the $1.40 * (\lambda/4)$ and $1.11 * (\lambda/4)$ extended cavity lengths reveal asymmetry, $(\lambda/4)$ type resonant MIM modes are supported in either case of anterior and exterior side illumination (see Figure A3(bc) in Appendix A). The **E**-field is enhanced at the entrance of nano-cavities and at cavity-side corners of both deflectors (Figure 4(cc)). Caused by increased periodicity, double-deflector array cannot expel the **E**-field from the region in between them. As a consequence, clockwise power-flow vortices are noticeable under the interleaved gold segments. The **E**-field time-evolution shows standing waves, however with time-dependent intensity (see Multimedia file 9). These standing waves originate from the co-existent forward and backward propagating plasmonic surface modes coupled in $+1$ and -1 order on the integrated pattern, which ensure that the neighboring nano-cavities are almost synchronously illuminated. The right phase-shift is introduced by the slightly different $1.40 * (\lambda/4)$ and $1.11 * (\lambda/4)$ extended nano-cavity lengths, and the time evolution of **E**-field compensates the asymmetry of deflectors. In the scattered-field region, the decay of these standing modes rather than

reflected light is observable. The $1.34 * 10^{-3}$ NbN/Au volume fraction ratio is further reduced, so the achievement of large NbN absorptance can be understood by taking the near-field distribution into account (see Appendix Figure A3(cc)). According to slightly larger NbN/Au volume-fraction-ratio, larger absorptance is achievable than in NCDAI$_\lambda$-A.

In optimized NCTAI$_{1/2*\lambda}$-A, both the nano-cavity width and length are decreased. The $0.57*(\lambda/4)$ length of nano-cavities is significantly smaller than quarter-wavelength, which reveals that the MIM modes are more strongly squeezed than in NCAI$_{1/2*\lambda}$-A (see Figure A4(ba) in Appendix A). At the global absorptance maximum **E**-field enhancement is observable both at the anterior and exterior sides of the cavities, and at the anterior side of trenches (Figure 4(da)). The Poynting vectors indicate a power-flow towards the entrance of nano-cavities, and the time-averaged **E**-field is negligible inside the trench. The neighboring cavities and the inserted trench are lightened successively (see Multimedia file 10). The backward propagating waves are only weakly observable caused by co-existent intense reflected waves. The $4.53 * 10^{-3}$ NbN/Au volume fraction ratio is the largest among half-wavelength-scaled devices (see Appendix Figure A4(ca)). In spite of larger NbN/Au volume-fraction-ratio, the **E**-field enhancement is slightly weaker, and the resulting absorptance is slightly smaller than in NCDDAI$_{1/2*\lambda}$-A. This can be explained by that one degree of freedom, namely that related to deflector's length difference, which is important in phase compensation, is not at play during NCTAI-A optimization.

In the optimized NCTAI$_{3/4*\lambda}$-A device, the $0.69 * (\lambda/4)$ cavity length is smaller than quarter wavelength; however, the squeezing of localized modes resonant in the MIM nano-cavities is smaller than the squeezing in NCTAI$_{1/2*\lambda}$-A (see Figure A4(bb) in Appendix A). The **E**-field distribution is very similar to that in NCTAI$_{1/2*\lambda}$-A (Figure 4(db)). The Poynting vector indicates a power-flow towards the nano-cavities, and the **E**-field is completely expelled from the region of trenches. The neighboring cavities are illuminated alternately, while the trench is lightened almost continuously (see Multimedia file 11). Well-defined backward propagating waves are observable, which originate from -1 order coupling. The $3.60 * 10^{-3}$ NbN/Au volume fraction ratio is the largest among three-quarter-wavelength scaled devices (see Figure A4(cb) in Appendix A). The **E**-field enhancement and the resulting absorptance are larger than in NCDDAI$_{3/4*\lambda}$-A, in accordance with two-times larger NbN/Au volume-fraction-ratio.

In the optimized NCTAI$_\lambda$-A, the $0.72*(\lambda/4)$ nano-cavity length indicates that the resonant modes are less squeezed, when the periodicity of in-plane vertical gold segments is wavelength-scaled (see Appendix Figure A4(bc)). The **E**-field is enhanced significantly at the entrances of nano-cavities, while at the trench corners only smaller enhancement is observable (Figure 4(dc)). The Poynting vector shows strong perpendicular power-flow towards the NbN segments. Standing waves are observable, which originate from the co-existent forward and backward propagating coupled modes. As a result, the neighboring cavities and inserted trenches are illuminated alternately (see Multimedia file 12). The **E**-field enhancement is significant around NbN segments in dominant parts of the duty-cycles. As a result, high absorptance enhancement is achieved in the NCTAI$_\lambda$-A, in accordance with the two-times larger $2.66 * 10^{-3}$ NbN/Au volume-fraction-ratio compared to NCDDAI$_\lambda$-A, which is the largest among wavelength-scaled devices (see Appendix Figure A4(cc)). The absorptance enhancement is the highest in NCTAI$_\lambda$-A in spite of the fact that the NbN/Au volume fraction ratio is reduced compared to other NCTAI-A devices.

3.3. Polarization Contrast Attainable via A-SNSPDs

High polarization contrast is crucial in numerous quantum information processing applications [34, 35]. In A-SNSPD type devices, the polarization contrast exponentially increases by increasing tilting almost throughout the complete polar angle interval, except the regions, where it is modulated dominantly by the polar-angle-dependent NbN absorptance of p-polarized light (Figures 5(a)–(d)). One exception is the NCTAI$_\lambda$-A, where the polarization first decreases at small polar angle and after a global minimum increases exponentially.

Figure 5(a) indicates that the polarization contrast of NCAI$_{1/2*\lambda}$-A is 19.28 at perpendicular incidence and increases monotonically exponentially. The increase is less significant in this device, and the polarization contrast reaches 240.92 at 85.00°. On the polarization contrast of NCAI$_{3/4*\lambda}$-A, a significant modulation appears at $\sim 15.60°$ tilting according to the global minimum in p-polarized light absorptance. At perpendicular incidence, the polarization contrast is slightly smaller than in NCAI$_{1/2*\lambda}$-

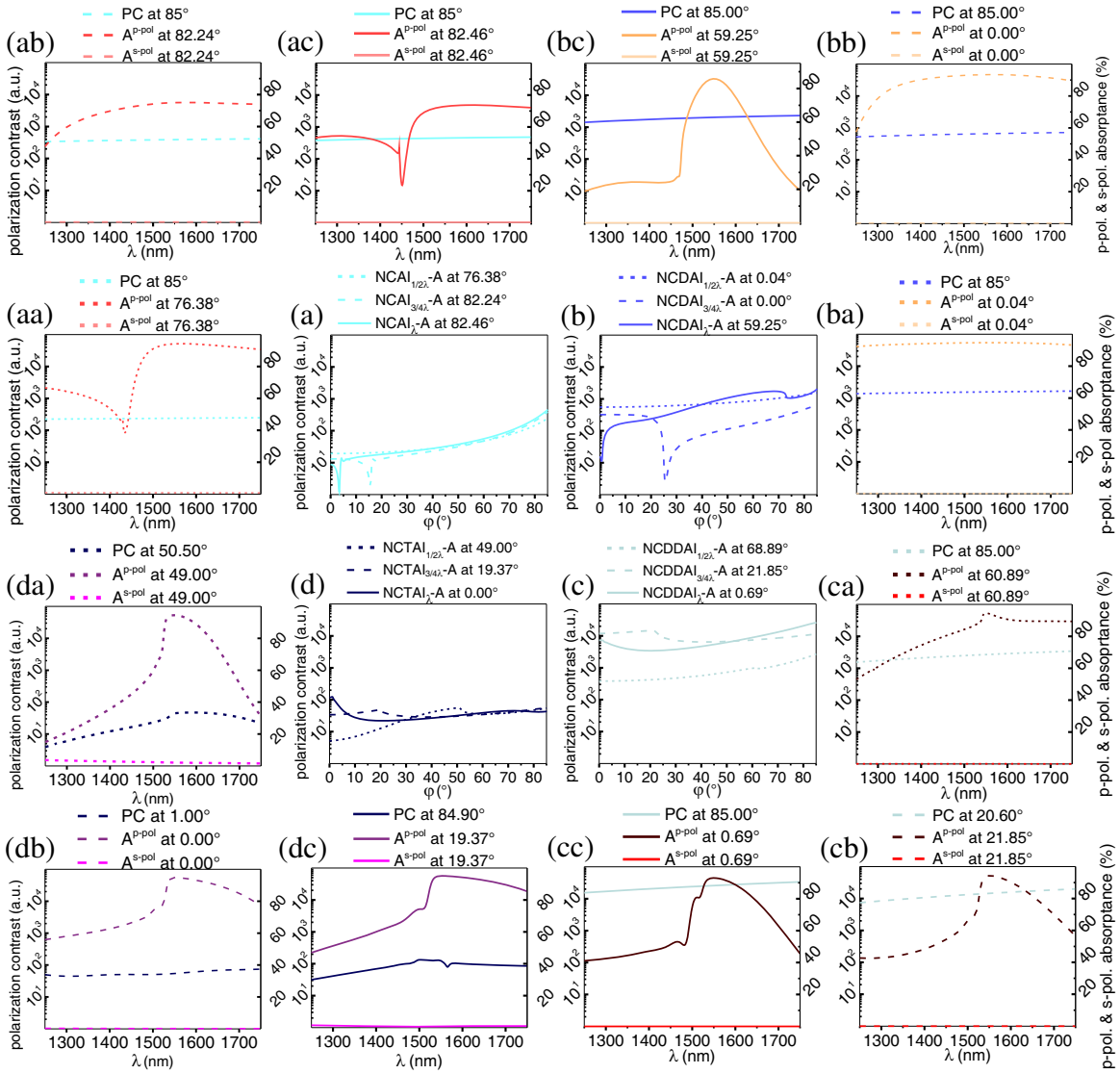

Figure 5. Polar-angle-dependent polarization contrast achievable via (a) NCAI-, (b) NCDAI-, (c) NCDDAI- and (d) NCTAI-A-SNSPD. Wavelength-dependent polarization contrast (PC) at contrast maxima and wavelength-dependent p-polarized ($A^{p\text{-}pol}$) and s-polarized ($A^{s\text{-}pol}$) absorptance at absorptance maxima in (aa) $NCAI_{1/2*\lambda}$-, (ab) $NCAI_{3/4*\lambda}$-, (ac) $NCAI_{\lambda}$-, (ba) $NCDAI_{1/2*\lambda}$-, (bb) $NCDAI_{3/4*\lambda}$-, (bc) $NCDAI_{\lambda}$-, (ca) $NCDDAI_{1/2*\lambda}$-, (cb) $NCDDAI_{3/4*\lambda}$-, (cc) $NCDDAI_{\lambda}$-, (da) $NCTAI_{1/2*\lambda}$-, (db) $NCTAI_{3/4*\lambda}$- and (dc) $NCTAI_{\lambda}$-A-SNSPD.

A, but increases with a larger rate through 389.45 at 85°. The course of polarization contrast in $NCAI_{\lambda}$-A is similar to that of $NCAI_{3/4*\lambda}$-A, and the only significant difference is the shift of modulation towards smaller polar angles. Although at perpendicular incidence the contrast is smaller than in the two previous devices, it reaches 450.35 value at 85.00°, which is the largest among NCAI-SNSPDs. The parallel exponential decrease of s-polarized absorptance in S-orientation suppresses the modulation originating from PBA on the p-polarized absorptance of NCAI-A-SNSPDs.

In deflector-array integrated NCDAI-SNSPDs, the polarization contrast overrides those in counterpart NCAI-SNSPDs throughout dominant part of the inspected polar-angle interval, which proves the polarization selective role of deflectors (Figure 5(b)). In $NCDAI_{1/2*\lambda}$-A, the polarization contrast is an order of a magnitude higher than in the counterpart $NCAI_{1/2*\lambda}$-A device. At perpendicular

incidence, the contrast is 552.68 and increases exponentially through 1552.96 at 85.00°, without any significant modulation. In NCDAI$_{3/4*\lambda}$-A, the contrast is $\sim$ 300 in the 0.00°–20.00° polar-angle interval, according to the plateau in polar-angle-dependent absorptances. At $\sim$ 25.50° orientation corresponding to the cut-off in *p*-polarized absorptance, a global minimum arises, then the contrast increases and reaches 656.51 at 85.00°. In NCDAI$_{\lambda}$-A, the polarization contrast is 15.86 at perpendicular incidence and rapidly increases in a 2° interval according to the same characteristics of the *p*-polarized absorptance. By increasing tilting, the contrast increases through the 2029.44 global maximum at 85.00°.

In double-deflector integrated NCDDAI-SNSPDs, the polarization contrast is further enhanced (Figure 5(c)). In NCDDAI$_{1/2*\lambda}$-A at perpendicular incidence, the 381.07 contrast is less than in NCDAI$_{1/2*\lambda}$-A, but increases monotonically exponentially trough 2678.96 at 85.00°. In NCDDAI$_{3/4*\lambda}$-A, significantly larger polarization contrast is reachable. The contrast is 11915.59 already at perpendicular incidence and increases monotonically until 20.60°, where it reaches a global maximum of 14498.44. After this global maximum, a small reduction occurs originating mainly from the course of polar-angle-dependent *p*-polarized absorptance, then the contrast increases slightly according to more rapid exponential decrease of *s*-polarized absorptance. In NCDDAI$_{\lambda}$-A, the contrast is 7254.79 already at perpendicular incidence, then decreases according to the relative slopes of *p*- and *s*-polarized absorptance. After a global minimum of 3426.28 at 20.1°, the contrast increases through 25853.17 at 85.00°.

The trench array integrated NCTAI-SNSPDs result in the smallest polarization contrast indicating that embedded trenches enhance the absorptance via less polarization selective phenomena (Figure 5(d)). In NCTAI$_{1/2*\lambda}$-A, the contrast is 5.16 at perpendicular incidence and reaches its global maximum of 55.31 at 50.50° according to the large maximum on the polar-angle-dependent *p*-polarized absorptance. In NCTAI$_{3/4*\lambda}$-A, the contrast is 33.88 at perpendicular incidence and increases monotonically until 19.9°, where a global/local maximum is observable in absorptance/contrast. Finally, the contrast reaches its global maximum of 54.63 at 84.90°. In NCTAI$_{\lambda}$-A, the contrast shows a global maximum of 123.75 at 1.00°, then begins to decrease rapidly according to the polar-angle-dependent absorptance. After a global minimum at 20.9°, the contrast exhibits 45.19 local maximum at 72.00°.

3.4. Bandwidth Corresponding to Maxima in Absorptance and in Polarization Contrast Achievable via Optimized A-SNSPD Configurations

On the wavelength-dependent p-polarized absorptance at tilting corresponding to the plasmonic Brewster angle of NCAI-A devices, a cut-off is observable in the inspected region (Figures 5(b)/(a)–(c)). The cut-off in NCAI$_{1/2*\lambda}$-A corresponds to the first Wood-anomaly ($d(\sin\varphi + \sin 90°) = 1 * \lambda$), in accordance with the literature (Figure 5(aa)) [63]. Our present work demonstrates that in NCAI$_{\lambda}$-A device having two times larger periodicity a similar cut-off originating from second Wood-anomaly arises ($2 * d(\sin\varphi + \sin 90°) = 2 * \lambda$) (Figures 5(a)–(c)).

At tilting corresponding to maxima in polar angle, the NbN absorptance is almost wavelength-independent in NCDAI$_{1/2*\lambda}$-A, and a cut-off is observable at the small wavelength edge of the inspected interval in NCDAI$_{3/4*\lambda}$-A, while the NCDAI$_{\lambda}$-A has a discrete plasmonic pass band revealing to polarization specific filtering capability [64] (Figure 5(b)/(a)–(c)).

In all NCDDAI-SNSPD devices, the wavelength-dependent absorptance indicates a plasmonic pass band at tilting corresponding to maxima in polar angle, which is the broadest and exhibits a small cut-off in NCDDAI$_{1/2*\lambda}$-A, asymmetrical caused by a well-defined cut-off in NCDDAI$_{3/4*\lambda}$-A, and almost symmetrical in spite of a double cut-off in NCDDAI$_{\lambda}$-A, revealing that different phenomena result in polarization specific filtering capability inside bands of different width (Figures 5(c)/(a)–(c)) [64].

The absorptance at tilting corresponding to maxima in polar angle shows a wavelength dependency in NCTAI-SNSPDs, which is very similar to that of NCDDAI-A-SNSPDs. Plasmonic pass band appears in each NTCAI-A, which indicates a noticeable cut-off in NCTAI$_{1/2*\lambda}$-A. A more well-defined cut-off is observable in NCTAI$_{3/4*\lambda}$-A, and similar cut-off appears in NCTAI$_{\lambda}$-A. The full-width at half maximum of the band in NCTAI$_{\lambda}$-A overrides that in NCDDAI$_{\lambda}$-A proving that NCTAI$_{\lambda}$-A acts as an almost perfect absorber in very broadband of several hundred nanometers (Figures 5(d)/(a)–(c)).

Moreover, the polarization contrast does not indicate significant wavelength dependency in any A-SNSPD devices at tilting corresponding to maxima in polar angle, i.e., commensurate polarization selectivity is preserved trough wide bands.

4. DISCUSSION AND CONCLUSION

In case of the simplest NCAI-A-SNSPDs light tunneling at the PBA enhances the collective resonance on the nano-cavity-grating composed of MIM nano-cavities, which are slightly shorter than quarter wavelength. The maximal absorptance achieved in NCAI-SNSPD devices is determined by the **E**-field enhancement attainable at the PBA corresponding to NbN loaded nano-cavities. The tunneling phenomenon is capable of ensuring large absorptance enhancement at well-defined polar-angle in wide wavelength interval (Figures 2(a), 3(a), 4(a), 5(a)). The optimal orientations are in accordance with the pitch dependence of PBA (see Figures A1 (a)/(a)–(c) in Appendix A), namely locations of global maxima correspond to $\cos\theta_{Brewster} = \beta w/k_0 p$ tilting, where k_0 and β are the propagation constants of photonic and MIM modes, and w is the nano-cavities width and p the periodicity [42–44]. The absorptance is almost polar-angle-independent in $NCAI_{1/2*\lambda}$-A according to the sub-wavelength pitch [45–48], while grating coupling related modulations resulting in Wood-anomaly features perturb the absorptance in $NCAI_{3/4*\lambda}$-A and $NCAI_{\lambda}$-A [31, 33, 49–56]. The observed wavelength dependency at the large absorptance maxima arising at PBA indicates that it is possible to set the cut-off at the first and second Wood anomalies in $NCAI_{3/4*\lambda}$-A and $NCAI_{\lambda}$-A outside the region of interest via an appropriate design [63]. By increasing the periodicity of NCAI-A devices, the NbN/Au volume fraction ratio gradually decreases (see Figures A1(c)/(a)–(c) in Appendix A), while the achieved absorptance rapidly decreases (see Figure A1(a) in Appendix A). The optimal integrated device geometry is $NCAI_{3/4*\lambda}$-A based on the highest attainable 94.18% absorptance via 500 nm periodic NbN pattern at 76.38° tilting.

Important advantage is that all NCAI-A-SNSPDs are based on in-plane pattern, which indicates their experimental feasibility. The absorptance might be further enhanced not only in a wide spectral band, but also in a wide polar-angle interval by applying tilted cavity walls and conical MIM cavity shapes in NCAI-A-SNSPDs [63, 65]. However, inspection of tilted walls was outside the scope of present optimization studies. From the point of view of practical applications, the challenge in the case of NCAI-A-SNSPDs is that to reach the PBA, a special in-coupling methodology, e.g., trough slant-cut optical fibers, is necessary. In addition to this, the achievable polarization contrast is limited to 10^2 order of magnitude.

The collective resonances occur inside wide plasmonic bands in nano-cavities extended by the inserted deflectors to quarter/three-times quarter wavelength in $NCDAI_{1/2*\lambda}$-A and $NCDAI_{3/4*\lambda}$-A/$NCDAI_{\lambda}$-A-SNSPD. The significantly different optimal orientations reveal that various nanophotonical phenomena are at play in different periodicity intervals (see Figures A2(a)/(a)–(c) in Appendix A). In the case of $NCDAI_{1/2*\lambda}$-A, the collective resonance is capable of ensuring large absorptance throughout the largest polar-angle and wavelength interval among all inspected devices (Figures 3(ba), 5(ba)) [45–48]. In $NCDAI_{3/4*\lambda}$-A, the grating coupling in -1 order into Brewster-Zenneck type waves results in a cut-off (Figures 3(bb), 5(bb)) [49–53, 57–61]. In $NCDAI_{\lambda}$-A, grating coupling in -2 order into backward propagating modes enhances the absorptance well before the second Brillouin zone boundary (Figures 3(bc), 5(bc)). The surprisingly small 975.45 nm coupled mode wavelength is determined by the interplay of a plasmonic band and the PBA phenomenon corresponding to the wide cavity arising between successive deflectors. The 55.55° PBA originating from deflector-array approximates 59.25° tilting corresponding to the NbN absorptance maximum. At tilting corresponding to maximal absorptance of $NCDAI_{\lambda}$-A, the cut-off at small wavelength is coincident with the second Wood anomaly, and the resulted bandwidth is small in spite of the nearby PBA originating from cavities in between deflectors. The NbN/Au volume fraction ratio more rapidly decreases with the periodicity in the presence of deflectors (see Figures A2(c)/(a)–(c) in Appendix A). Accordingly, the achieved absorptance gradually decreases (see x Figure A2(a) in Appendix A). The optimal integrated device geometry is $NCDAI_{1/2*\lambda}$-A based on the highest attainable 94.68% absorptance via 500.09 nm periodic integrated pattern at 0.04° tilting.

The absorptance achieved via $NCDAI_{1/2*\lambda}$-A is larger than in $NCAI_{1/2*\lambda}$-A in spite of gold deflectors presence, and the appearance of the global maximum at almost perpendicular incidence is also preferred in applications. The most important advantage of the NCDAI-A-SNSPD devices is that large absorptance is achievable in the widest polar-angle and wavelength interval in all inspected periodicity regions. The small optimal polar angles as well as tilting insensitivity is particularly important in practical applications. These NCDAI-A-SNSPD studies suggest that better absorptance

can be achieved, only when the grating coupling related maximum is coincident with PBA corresponding to NbN loaded nano-cavity-array. Under these circumstances, besides co-existent grating coupling and light tunneling, the wavelength independency of PBA can be preserved. All NCDAI-A devices exhibit well-defined polarization-dependent filtering capability, allowing reaching $10^2 - 10^3$ contrast through wide bands, which can be tailored by the integrated device design [64]. The challenge in the case of NCDAI-SNSPD designs is that they consist of penetrating gold segments, whose fabrication requires two-step lithography with a synchronization in between them.

The collective resonances occur inside fundamentally different plasmonic bands in nano-cavities extended by the inserted double deflectors to quarter-/half-wavelength in NCDDAI$_{1/2*\lambda}$-A and NCDDAI$_{\lambda}$-A/NCDDAI$_{3/4*\lambda}$-A. Accordingly, in all of NCDDAI-A-SNSPD type devices, the coupling into plasmonic surface modes results in commensurately large global maxima, however at significantly different tilting (Figure 2(c)). The optimal polar angle very rapidly decreases with the periodicity, which indicates that different grating coupling phenomena act in different periodicity regions (see Figures A3(a)/(a)–(c) in Appendix A). In half- and quarter-wavelength-scaled periodic integrated devices, the backward propagating surface waves coupled in -1 order are capable of resulting in enhanced absorptance (Figures 3(ca), 3(cb), 5(ca), 5(cb)). Moreover, strong-coupling between collectively resonating nano-cavity and propagating modes is also observable in NCDDAI$_{1/2*\lambda}$-A, which results in larger absorptance enhancement than that originating separately from resonances of either modes (Figures 3(ca), 5(ca)) [62, 66]. The global maximum appears at 60.89°, which is close to 55.39° tilting, where the plasmonic band overlaps with PBA phenomenon corresponding to array of cavities arising between the longer exterior-side deflectors. Similarly, in NCDDAI$_{3/4*\lambda}$-A, a plasmonic pass band determined maximum appears at 21.85° tilting, which is just slightly smaller than the 32.01° PBA originating from the cavity arising between the longer exterior-side deflectors (Figures 3(cb), 5(cb)). In NCDDAI$_{\lambda}$-A, the double-deflector grating couples in 1 and -1 orders into forward and backward propagating modes, which enhance the absorptance at the top of the first Brillouin zone inside an inverted minigap (Figures 3(cc), 5(cc)) [49]. In all NCDDAI-A at tilting corresponding to maximal absorptance, the cut-off at small wavelength is coincident with the first Wood anomaly. However, the bandwidth is again narrowed in spite of nearby PBAs originating from cavities arising in between the longer exterior-side deflectors in NCDDAI$_{1/2*\lambda}$-A and NCDDAI$_{3/4*\lambda}$-A. By increasing the periodicity of NCDDAI-A devices, the NbN/Au volume fraction ratio gradually decreases (see Figures A3(c)/(a)–(c) in Appendix A). Accordingly, the achieved absorptance slowly decreases (see Figure A3(a) in Appendix A). The optimal integrated device geometry is half-wavelength-scaled also in the case of NCDDAI-SNSPD. The highest 94.60% absorptance is attained via 500.09 nm periodic NbN pattern at 60.89°. Although the 94.34% global maximum does not override the 94.60% attainable via NCDDAI$_{1/2*\lambda}$-A, the NCDDAI$_{3/4*\lambda}$-A device has a smaller kinetic inductance and so shorter reset time. In addition to this, NCDDAI$_{\lambda}$-A devices resulting in slightly smaller absorptance at almost perpendicular incidence and ensuring competitive kinetic inductance are also promising for special application purposes.

Practical advantage of the NCDDAI-A-SNSPD devices is that the large absorptance is achievable at gradually decreasing polar angle. Flat bands can be tailored by ensuring better overlap between plasmonic bands and PBA phenomenon corresponding to NbN loaded nano-cavity-array also in NCDDAI-A-SNSPD devices. Inspection of tilted cavity and deflector walls and conical extended cavities is the subject of further studies [63, 65]. All NCDDAI-A exhibit well defined polarization-dependent filtering capability, allowing reaching $10^3 - 10^4$ contrast inside finite bands, whose width strongly depends on the periodicity [64]. The challenge in the case of NCDDAI-A-SNSPD devices is that they consist of two different penetrating segments, whose fabrication requires three successive steps.

The NCDAI-A and NCDDAI-A devices can be considered as multi-component diffraction gratings, which can have unique plasmonic band structure and can exhibit strong absorption at specific wavelength in the case of optimized design [67–69]. Further research is in progress to replace deflectors, with in-plane multi-component gratings.

The collective resonances in nano-cavities shorter than quarter-wavelength occur inside fundamentally different plasmonic bands in NCTAI-A-SNSPDs. Accordingly, the coupling on the periodic NCTAI-SNSPD type grating profiles results in appearance of plasmonic pass-bands and in large global maxima, however at different tilting (Figures 3(d), 5(d)), namely the optimal tilting decreases monotonously by increasing the periodicity (see Figures A4(a)/(a)–(c) in Appendix A). Both

in NCTAI$_{1/2*\lambda}$-A and NCTAI$_{3/4*\lambda}$-A, the backward propagating surface waves coupled in -1 order are capable of resulting in enhanced absorptance (Figures 5(da), (db)). In NCTAI$_{1/2*\lambda}$-A, the absorptance maximum at 49.00° is close to 55.15° tilting, where the plasmonic band overlaps with PBA phenomenon corresponding to array of nano-cavities arising between the wider exterior deflectors. In NCTAI$_\lambda$-A grating couplings in 1 and -1 order into forward and backward propagating modes at the top of the first Brillouin zone result in the highest absorptance inside an inverted minigap (Figure 5(dc)) [49]. In all NCTAI-A at tilting corresponding to maximal absorptance, the cut-off at small wavelength is coincident with the first Wood anomaly. The bandwidth is narrowed in spite of nearby PBA originating from trenches in NCTAI$_{1/2*\lambda}$-A, while the bands are broader in the absence of PBA in NCTAI$_{3/4*\lambda}$ and NCTAI$_\lambda$-A. By increasing the periodicity of NCTAI-A devices, the NbN/Au volume fraction ratio slowly decreases (see Figures A4(c)/(a)–(c) in Appendix A). In contrast, the absorptance slowly increases (see Figure A4(a) in Appendix A). The considerably large NbN/Au volume fraction ratio makes it possible to achieve very high, almost perfect absorptance in NCTAI$_\lambda$-A-SNSPD. The optimal integrated device geometry is NCTAI$_\lambda$-A, and the 95.05% absorptance attained via 1042.83 nm periodic NbN pattern at 0.00° is the highest absorptance achieved in optimized SNSPDs. The achievement of absorptance maximum under these conditions is in contradiction with the literature describing that when the Rayleigh condition is met, a minimum in transmission and in corresponding absorption is expected [53–56]. Important property of the optimized NCTAI$_\lambda$-A that the kinetic inductance of the detector device is low which results in fast reset time. Further important parameter is that the global maximum appears at perpendicular incidence.

Common advantage of NCTAI-A-SNSPDs is that they consist of in-plane gold segments, exclusively, and the optimal polar angles are further reduced compared to corresponding NCDDAI-A-SNSPDs. The NCTAI-A devices can be considered as the simplest compound gratings [70, 71]. The effect of distributed gratings consisting of different periodic components as well as the possible advantages of tilted cavity and trench walls is a subject of further studies [63, 65]. The NCTAI-A-SNSPDs result in significantly smaller polarization contrast, on the order of $10 - 10^2$, and they are more orientation sensitive and act inside the narrowest bands. However, the achievable very large absortance is a reasonable argument to fabricate them.

In summary, our present work proves that maximization of absorptance in SNSPDs can be realized by optimizing the dispersion characteristics of plasmonic structure integrated devices. For QIP applications, important requirements are to increase secure communication rate of information encoded into polarization via polarization specific detection efficiency, and to promote high communication rate at specific polarization via decreased reset time. Based on our present studies, performances of these parameters are reasonably compromised via NCDAI$_\lambda$- and NCDDAI$_\lambda$-A-SNSPDs, which ensure high absorptance at specific polarization along with large contrast and short reset time due to reduced length. In A-SNSPD devices, the polarization contrast exponentially increases with the tilting and reaches its maximum at 85.00° in most of the inspected device types, and exceptions are the NCDDAI$_{3/4*\lambda}$-A and NCTAI-A-SNSPDs. The wavelength insensitivity of the polarization contrast is advantageous; however, the large tilting necessary to reach maximal polarization contrast is a drawback. When higher polarization contrast is required, C-SNSPD device configurations optimized with conditional absorptance offer a reasonable compromise. These devices are presented in Appendix A. Analyses of nanophotonical phenomena in P-SNSPD devices, which are optimized to ensure maximal polarization contrast, are in progress.

ACKNOWLEDGMENT

This work was supported by the European Union and European Social Fund through project ELITeam — Establishment of the ELI Institute at the University of Szeged: foundation of interdisciplinary research in the field of lasers and their applications (Project number: TÁMOP-4.2.2.D-15/1/KONV-2015-0024). The research was supported by National Research, Development and Innovation Office-NKFIH through project "Optimized nanoplasmonics" K116362. Mária Csete acknowledges that the project was supported by the János Bolyai Research Scholarship of the Hungarian Academy of Sciences. Gábor Szabó acknowledges the support of Hungarian Academy of Sciences. The authors would like to thank Dávid Maráczi for figures preparation.

APPENDIX A.

To provide an acceptable compromise between the achievable absorptance and polarization contrast (PC), we have specified criteria regarding the minimal absorptance and inspected the achievable polarization contrast as well as the parameters of optimized C-SNSPD configurations, by gradually decreasing the conditional absorptance (CA). The criterion regarding the p-polarized absorptance, which have to be parallel met, was varied with 0.25% steps in 3% interval of the maximal absorptance previously determined for each specific A-SNSPD device type. The related nonlinearly constrained optimization problems were solved by a penalty function approach, and the obtained results clearly indicate that the constraints were satisfied [72].

A.1. NCAI-C-SNSPDs Capable of Maximizing the Polarization Contrast at Conditional Absorptance

In all NCAI-C-SNSPD devices, the polarization contrast slowly and monotonously increases by decreasing the conditional absorptance (Figure A1(a), Table A1: CA, $PC = A^{p\text{-}pol}/A^{s\text{-}pol}$). The period

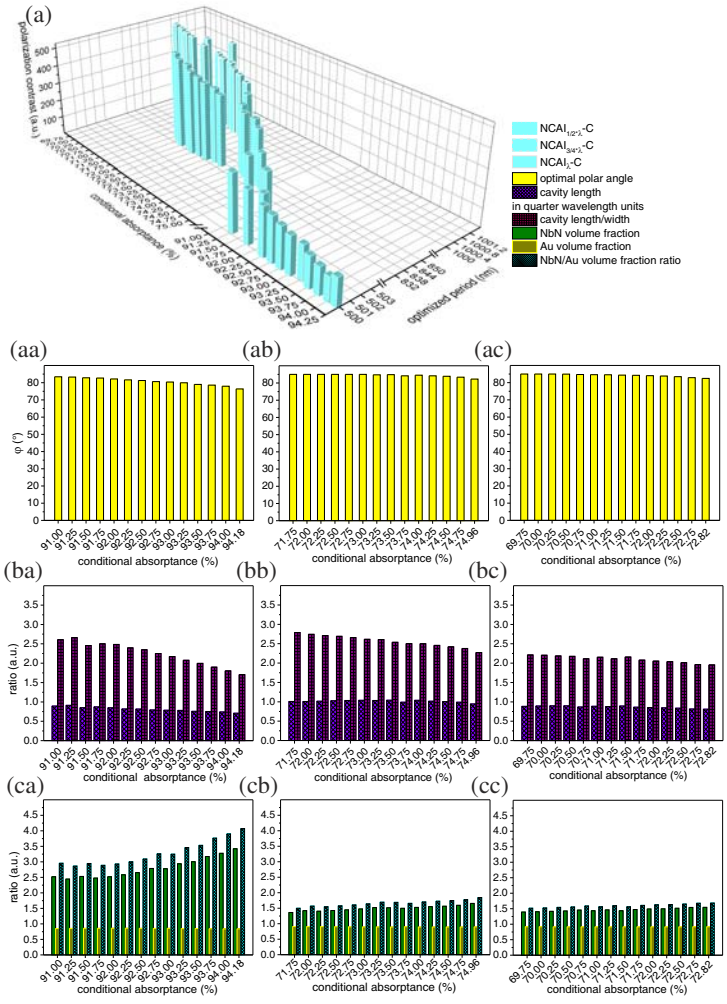

Figure A1. (a) Attained polarization contrast (PC), optimized period (p) and optimal polar angle (φ) as a function of conditional absorptance (CA). Histograms indicating tendencies of (b) cavity length in quarter wavelength units ($l/(\lambda/4)$) and cavity length/width (l/w) ratio qualifying MIM modes squeezing, (c) NbN and Au volume fraction, NbN/Au volume fraction ratio (V_{NbN}/V_{Au}), all as a function of conditional absorptance in (a)–(c)/(a) $NCAI_{1/2*\lambda}$-, (a)–(c)/(b) $NCAI_{3/4*\lambda}$-, (a)–(c)/(c) $NCAI_{\lambda}$-C-SNSPDs.

Table A1. Intervals, where parameters take on values during NCAI-C-SNSPD optimization. CA: conditional absorptance, PC: polarization contrast, p: optimized period, φ: optimal polar angle, $l/(\lambda/4)$: cavity length in quarter wavelength units, l/w: cavity length/width ratio, V_{NbN}/V_{Au}: NbN/Au volume fraction ratio.

-	*unit*	$1/2*\lambda$	$3/4*\lambda$	λ
CA	%	94.18–91.00	74.96–71.75	72.82–69.75
PC	*a.u.*	$1.26*10^2$–$3.20*10^2$	$3.08*10^2$–$5.12*10^2$	$3.32*10^2$–$4.88*10^2$
p	*nm*	500.00–502.61	836.18–835.09	1000.00–1000.02
φ	*deg*	76.38–83.42	82.24–85.00	82.46–85.00
$l/(\lambda/4)$	*a.u.*	0.71–0.89	0.95–1.01	0.81–0.88
l/w	*a.u.*	1.70–2.66	2.27–2.79	1.95–2.21
V_{NbN}/V_{Au}	*a.u.*	$4.07*10^{-3}$–$2.96*10^{-3}$	$1.85*10^{-3}$–$1.50*10^{-3}$	$1.68*10^{-3}$–$1.52*10^{-3}$

slightly modifies close to the lower/upper/lower bounds of the optimization regions in $\text{NCAI}_{1/2*\lambda}$-/$\text{NCAI}_{3/4*\lambda}$-/$\text{NCAI}_{\lambda}$-C-SNSPD (Figure A1(a): y-axes, Table A1: p). All optimal polar angles correspond to the PBA. By decreasing the conditional absorptance their value increases slowly (Figures A1(a)/(a)–(c), Table A1: φ). The cavity lengths non-monotonously increase in all NCAI-C-SNSPDs (Figures A1(b)/(a)–(c), Table A1: $l/(\lambda/4)$). The type of MIM modes that are supported by NCAI-C-SNSPDS is quarter-wavelength. The cavity parameter tendencies result in monotonously increasing cavity length/width ratio, which reveals that the MIM modes become less confined in case of smaller conditional absorptance (Figures A1(b)/(a)–(c), Table A1: l/w). The NbN/Au volume fraction ratio almost monotonously decreases by decreasing the conditional absorptance (Figures A1(c)/(a)–(c), Table A1: V_{NbN}/V_{Au}).

A.2. NCDAI-C-SNSPDs Capable of Maximizing the Polarization Contrast at Conditional Absorptance

In each NCDAI-C-SNSPD device, the polarization contrast more rapidly and monotonously increases by decreasing the conditional absorptance (Figure A2(a), Table A2: CA, $PC = A^{p\text{-}pol}/A^{s\text{-}pol}$). The period

Table A2. Intervals, where parameters take on values during NCDAI-C-SNSPD optimization. CA: conditional absorptance, PC: polarization contrast, p: optimized period, φ: optmimized polar angle, $l/(\lambda/4)$: cavity length in quarter wavelength units, l/w: cavity length/width ratio, $l_{extended}/(\lambda/4)$: extended cavity length in quarter wavelength units, $l_{extended}/w$: extended cavity length/width ratio, V_{NbN}/V_{Au}: NbN/Au volume fraction ratio.

-	*unit*	$1/2*\lambda$	$3/4*\lambda$	λ
CA	%	94.68–91.50	93.34–90.25	85.77–82.50
PC	*a.u.*	$8.28*10^2$–$3.02*10^7$	$3.96*10^2$–$1.90*10^3$	$1.75*10^3$–$5.03*10^3$
p	*nm*	500.09–500.24	754.61–750.35	1093.02–1064.08
φ	*deg*	0.04–71.33	0.00–40.26	59.25–75.65
$l/(\lambda/4)$	*a.u.*	0.59–0.64	0.49–0.98	1.00–0.85
l/w	*a.u.*	1.43–2.68	1.19–2.89	2.28–2.72
$l_{extended}/(\lambda/4)$	*a.u.*	1.22–2.51	1.04–1.69	2.38–2.50
$l_{extended}/w$	*a.u.*	2.96–6.17	2.51–4.97	5.74–7.34
V_{NbN}/V_{Au}	*a.u.*	$3.29*10^{-3}$–$1.67*10^{-3}$	$2.35*10^{-3}$–$1.16*10^{-3}$	$8.89*10^{-4}$–$7.07*10^{-4}$

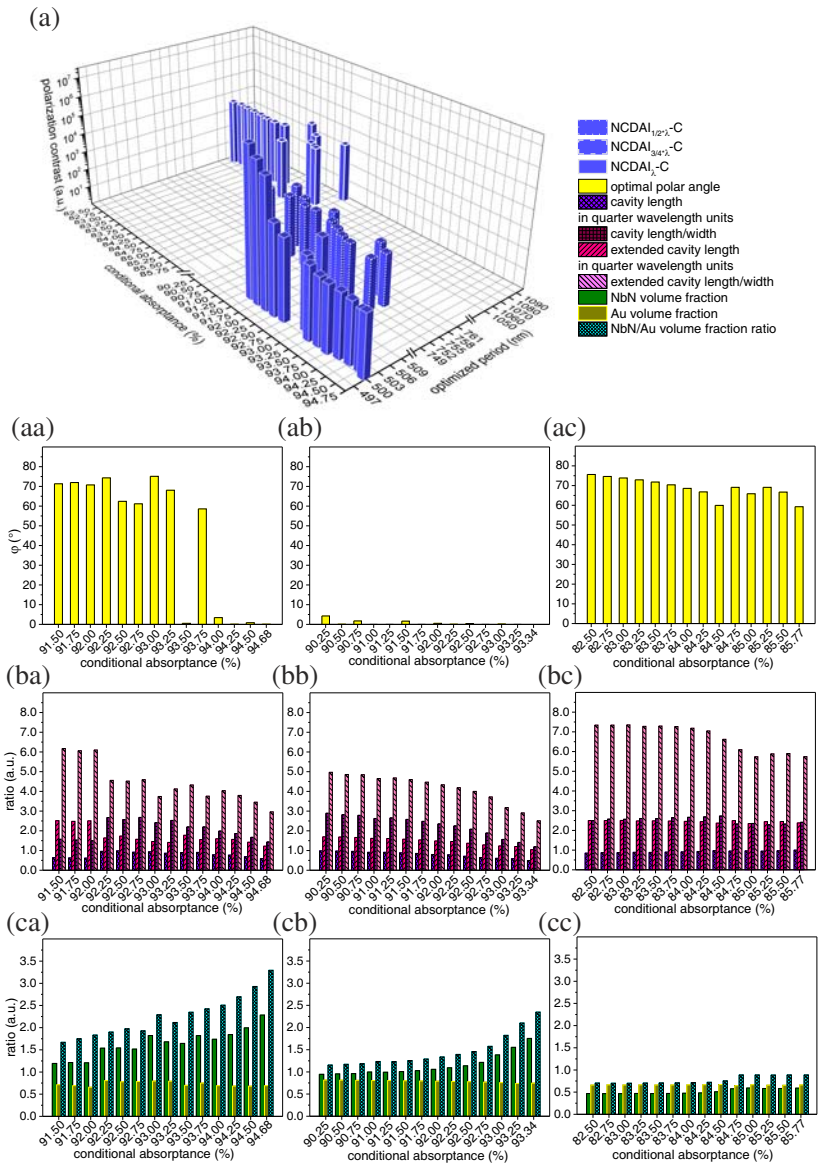

Figure A2. (a) Attained polarization contrast (PC), optimized period (p) and optimal polar angle (φ) as a function of conditional absorptance (CA). Histograms indicating tendencies of (b) cavity length in quarter wavelength units ($l/(\lambda/4)$), cavity length/width (l/w), extended cavity length in quarter wavelength units ($l_{extended}/(\lambda/4)$), and extended cavity length/width ($l_{extended}/w$) ratio qualifying MIM modes squeezing, (c) NbN and Au volume fraction, NbN/Au volume fraction ratio (V_{NbN}/V_{Au}), all as a function of conditional absorptance in (a)–(c)/(a) $NCDAI_{1/2*\lambda}$-, (a)–(c)/(b) $NCDAI_{3/4*\lambda}$-, (a)–(c)/(c) $NCDAI_{\lambda}$-C-SNSPDs.

non-monotonously varies close to the lower/upper bounds of the optimization regions in $NCAI_{1/2*\lambda}$- and $NCAI_{3/4*\lambda}$-/$NCAI_{\lambda}$-C-SNSPD (Figure A2(a): y-axes, Table A2: p). In $NCDAI_{1/2*\lambda}$-C-SNSPD, the optimal polar angle jumps in wide tilting region, indicating that different nanophotonical phenomena become to play to ensure conditional absorptance below a certain conditional absorptance level. In $NCDAI_{3/4*\lambda}$-C-SNSPD approximately zero is the optimal incidence, while in $NCDAI_{\lambda}$-C-SNSPD large tilting is preferred (Figures A2(a)/(a)–(c), Table A2: φ).

The cavity length exhibits a maximum in $NCDAI_{1/2*\lambda}$-C-SNSPD/increases monotonously in $NCDAI_{3/4*\lambda}$-C-SNSPD, while decreases in $NCDAI_{\lambda}$-C-SNSPD (Figures A2(b)/(a)–(c), Table A2:

$l/(\lambda/4)$). The cavity parameter tendencies result in cavity length/width ratio, which exhibits a maximum in NCDAI$_{1/2*\lambda}$- and NCDAI$_{\lambda}$-C-SNSPD, and shows a monotonous increase in NCDAI$_{3/4*\lambda}$-C-SNSPD, respectively (Figures A2(b)/(a)–(c), Table A2: l/w). The extended cavity length exhibits non-monotonous increase in NCDAI$_{1/2*\lambda}$- and in NCDAI$_{\lambda}$-C-SNSPD, while slow monotonous increase can be seen in NCAI$_{3/4*\lambda}$-C-SNSPD (Figures A2(b)/(a)–(c), Table A2: $l_{extended}/(\lambda/4)$). The type of MIM modes that are supported by extended cavities modifies from quarter- to three-times quarter-wavelength in NCDAI$_{1/2*\lambda}$-C-SNSPD, from quarter- to half-wavelength in NCDAI$_{3/4*\lambda}$-C-SNSPD, while remains three-quarter-wavelength in NCDAI$_{\lambda}$-C-SNSPD (Figures A2(b)/(a)–(c), Table A2: $l_{extended}/(\lambda/4)$). The deflectors presence manifests itself in non-monotonous/almost monotonous increase in extended cavity length/width ratio in NCDAI$_{1/2*\lambda}$-/NCDAI$_{3/4*\lambda}$- and NCDAI$_{\lambda}$-C-SNSPD (Figures A2(b)/(a)–(c), Table A2: $l_{extended}/w$). The NbN/Au volume fraction ratio almost monotonously decreases in all NCDAI-C-SNSPD (Figures A2(c)/(a)–(c), Table A2: V_{NbN}/V_{Au}).

A.3. NCDDAI-C-SNSPD Capable of Maximizing the Polarization Contrast at Conditional Absorptance

In NCDDAI-C-SNSPD devices, the polarization contrast rapidly and monotonously increases by decreasing the conditional absorptance, except in NCDDAI$_{\lambda}$-C-SNSPD, where the increase is non-monotonous (Figure A3(a), Table A3: CA, $PC = A^{p\text{-}pol}/A^{s\text{-}pol}$). The period non-monotonously varies in all NCDDAI-SNSPDs (Figure A3(a): y-axes, Table A3: p). In NCDDAI$_{1/2*\lambda}$-C, the tilting non-monotonously varies, while in NCDDAI$_{3/4*\lambda}$-C slightly modifies and the optimal polar angle is almost independent of the conditional absorptance. The optimal polar angle exhibits a jump in NCDDAI$_{\lambda}$-C-SNSPD, indicating that different nanophotonical phenomena become to play below certain level of conditional absorptance (Figures A3(a)/(a)–(c), Table A3: φ).

The cavity lengths non-monotonously increase in all NCDDAI-C-SNSPDs (Figures A3(b)/(a)–(c), Table A3: $l/(\lambda/4)$). The cavity parameter tendencies result in non-monotonous cavity length/width ratio, which exhibits the most well-defined single maximum in NCDDAI$_{3/4*\lambda}$-C-

Table A3. Intervals, where parameters take on values during NCDDAI-C-SNSPD optimization. CA: conditional absorptance, PC: polarization contrast, p: optimized period, φ: optimized polar angle, $l/(\lambda/4)$: cavity length in quarter wavelength units, l/w: cavity length/width ratio, $l_{extended}^{anterior}/(\lambda/4)$: anterior extended cavity length in quarter wavelength units, $l_{extended}^{exterior}/(\lambda/4)$: exterior extended cavity length in quarter wavelength units, $l_{extended}^{anterior}/w$: anterior extended cavity length/width ratio, $l_{extended}^{exterior}/w$: exterior extended cavity length/width ratio, $V^{anterior}/V^{exterior}$: anterior/exterior deflector volume fraction ratio, V_{NbN}/V_{Au}: NbN/Au volume fraction ratio.

-	*unit*	$1/2*\lambda$	$3/4*\lambda$	λ
CA	%	94.60–91.50	94.34–91.25	93.00-89.75
PC	*a.u.*	$1.38*10^{3}$–$2.24*10^{9}$	$2.00*10^{4}$–$2.83*10^{8}$	$1.39*10^{4}$–$1.35*10^{10}$
p	*nm*	567.82–558.56	769.93–784.41	1042.83–1058.73
φ	*deg*	60.89–59.57	21.85–20.04	0.69–74.26
$l/(\lambda/4)$	*a.u.*	0.62–0.74	0.71–0.74	0.74–0.77
l/w	*a.u.*	1.53–2.71	1.84–2.28	1.78–2.74
$l_{extended}^{anterior}/(\lambda/4)$	*a.u.*	0.81–2.05	1.08–2.05	1.40–2.00
$l_{extended}^{exterior}/(\lambda/4)$	*a.u.*	1.09–2.54	1.75–2.63	1.11–2.66
$l_{extended}^{anterior}/w$	*a.u.*	2.00–5.97	2.79–5.28	3.39–6.52
$l_{extended}^{exterior}/w$	*a.u.*	2.69–7.39	4.51–7.12	2.69–7.82
$V^{anterior}/V^{exterior}$	*a.u.*	0.08–1.20	0.88–0.94	1.65–4.09
V_{NbN}/V_{Au}	*a.u.*	$3.08*10^{-3}$–$1.59*10^{-3}$	$1.74*10^{-3}$–$9.47*10^{-4}$	$1.34*10^{-3}$–$7.30*10^{-4}$

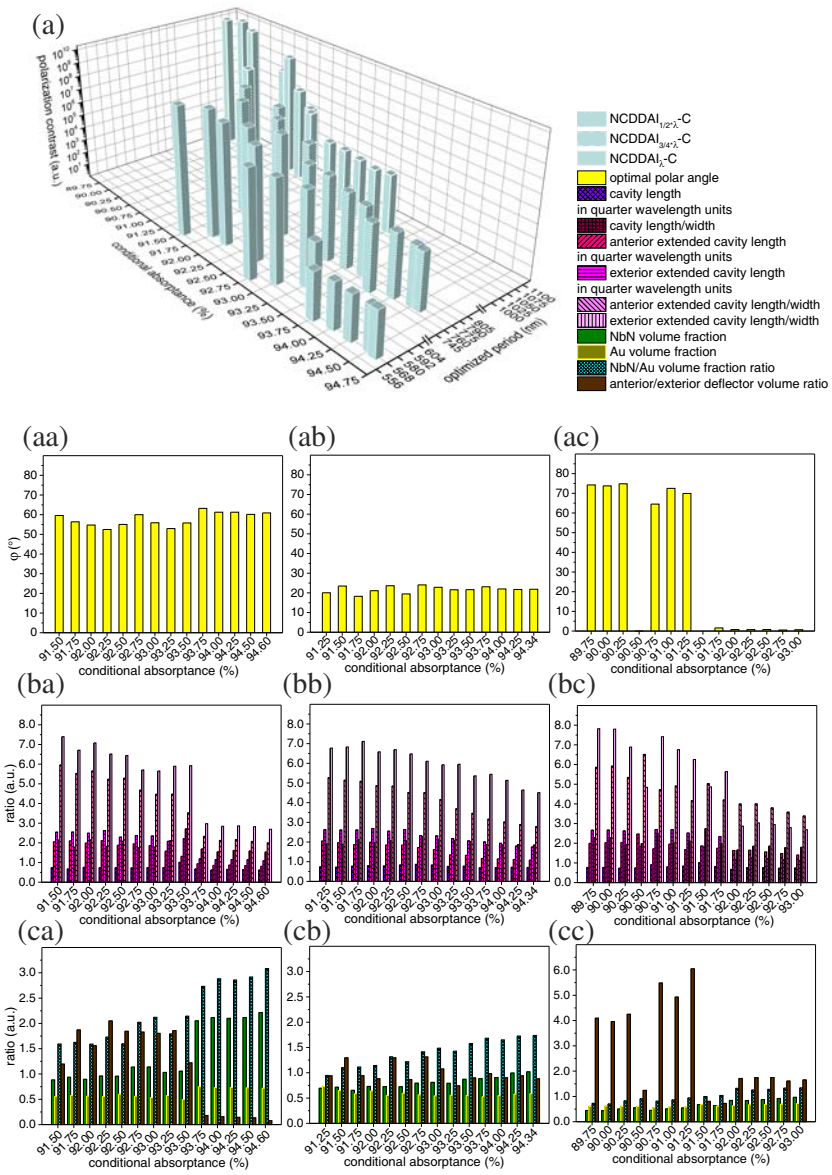

Figure A3. (a) Attained polarization contrast (PC), optimized period (p) and optimal polar angle (φ) as a function of conditional absorptance (CA). Histograms indicating tendencies of (b) cavity length in quarter wavelength units ($l/(\lambda/4)$), cavity length/width (l/w), anterior extended cavity length (($l^{anterior}_{extended}/(\lambda/4)$) and exterior extended cavity length ($l^{exterior}_{extended}/(\lambda/4)$) in quarter wavelength units, anterior extended cavity length/width ($l^{anterior}_{extended}/w$) and exterior extended cavity length/width ($l^{anterior}_{extended}/w$) ratio qualifying MIM modes squeezing, (c) NbN and Au volume fraction, NbN/Au volume fraction ratio (V_{NbN}/V_{Au}), anterior/exterior deflector volume fraction ratio ($V^{anterior}/V^{exterior}$), all as a function of conditional absorptance in (a)–(c)/(a) NCDDAI$_{1/2*\lambda}$-, (a)–(c)/(b) NCDDAI$_{3/4*\lambda}$-, (a)–(c)/(c) NCDDAI$_{\lambda}$-C-SNSPDs.

SNSPD (Figures A3(b)/(a)–(c), Table A3: l/w). The extended cavity lengths for both anterior and exterior deflector side illuminations exhibit almost monotonous increase in NCDDAI$_{1/2*\lambda}$- and NCDDAI$_{3/4*\lambda}$-C-SNSPD, while non-monotonous increase can be seen in NCDDAI$_{\lambda}$-C-SNSPD, respectively (Figures A3(b)/(a)–(c), Table A3: $l_{extended}/(\lambda/4)$). The type of MIM modes that are supported by extended cavities, when anterior side deflectors are illuminated, modifies from

quarter- to half-wavelength in all NCDDAI-C-SNSPDs. For illumination of exterior side deflectors, the MIM modes type modifies from quarter- to three-quarter-wavelength in NCDDAI$_{1/2*\lambda}$- and NCDDAI$_{\lambda}$-C-SNSPD, while in NCDDAI$_{3/4*\lambda}$-C-SNSPD half-wavelength-scaled mode is the original one. The deflectors presence manifests itself in a well-defined almost monotonous increase in extended cavity length/width ratio in all NCDDAI-C-SNSPDs (Figures A3(b)/(a)–(c), Table A3: $l_{extended}/w$). The ratio of deflectors at the anterior/exterior side of cavities increases rapidly/slowly/non-monotonously in NCDDAI$_{1/2*\lambda}$-/NCDDAI$_{3/4*\lambda}$-/NCDDAI$_{\lambda}$-C, respectively (Figures A3(c)/(a)–(c), Table A3: $V^{anterior}/V^{exterior}$). The NbN/Au volume fraction almost monotonously decreases in all NCDDAI-C-SNSPDs (Figures A3(c)/(c)–(a), Table A3: V_{NbN}/V_{Au}).

A.4. NCTAI-C-SNSPD Capable of Maximizing the Polarization Contrast at Conditional Absorptance

In NCTAI-C-SNSPD devices, the polarization contrast increases monotonously by decreasing the conditional absorptance, except in NCTAI$_{1/2*\lambda}$-C (Figure A4(a), Table A4: CA, $PC = A^{p\text{-}pol}/A^{s\text{-}pol}$). These results show that very low polarization contrast is achievable in the presence of trenches. The period non-monotonously varies in all NCTAI-C-SNSPDs (Figure A4(a): y-axes, Table A4: p). The optimal polar angle increases non-monotonously in NCTAI$_{1/2*\lambda}$-C, indicating again that significantly different nanophotonical phenomena are at play at different conditional absorptances. In NCTAI$_{3/4*\lambda}$-C and NCTAI$_{\lambda}$-C-SNSPD, the optimal tilting is almost independent of the conditional absorptance (Figures A4(a)/(a)–(c), Table A4: φ). The cavity length exhibits non-monotonous increase in all NCTAI-C-SNSPDs (Figures A4(b)/(c)–(a), Table A4: $l/(\lambda/4)$). The cavity lengths are smaller than quarter-wavelength in all NCTAI-C-SNSPD devices indicating that the resonant MIM modes are strongly confined. Accordingly, quarter-wavelength type resonant MIM modes are supported, and their wavelength gradually becomes similar to that of slightly squeezed SPP modes. Tendencies in geometrical parameters result in non-monotonous cavity length/width ratio except in NCTAI$_{3/4*\lambda}$-C, which exhibits an almost monotonous increase (Figures A4(b)/(a)–(c), Table A4: l/w). The ratio of deflectors on the anterior/exterior side of cavities modifies non-monotonously (Figures A4(c)/(c)–(a), Table A4: $V^{anterior}/V^{exterior}$). The NbN/Au volume fraction ratio is non-monotonous in all NCTAI-C devices (Figures A4(c)/(c)–(a), Table A4: V_{NbN}/V_{Au}).

In summary, configurations of C-SNSPD devices, which are capable of maximizing the polarization contrast at conditional absorptance, were determined for four different SNSPD device types in three periodicity intervals. Tendencies in configuration parameters ensuring polarization contrast maximization for different conditional absorptances show that in polarization contrast maximization enhancement of p-polarization, specific coupling phenomenon is dominant rather than squeezing of MIM

Table A4. Intervals, where parameters take on values during NCTAI-C-SNSPD optimization. CA: conditional absorptance, PC: polarization contrast, p: optimized period, φ: optimized polar angle, $l/(\lambda/4)$: cavity length in quarter wavelength units, l/w: cavity length/width ratio, $V^{anterior}/V^{exterior}$: anterior/exterior deflector volume fraction ratio, V_{NbN}/V_{Au}: NbN/Au volume fraction ratio.

-	*unit*	$1/2*\lambda$	$3/4*\lambda$	λ
CA	%	94.49–91.25	94.95–91.75	95.05–91.75
PC	*a.u.*	$5.53*10^{1}$–$1.91*10^{2}$	$6.21*10^{1}$–$7.73*10^{1}$	$1.55*10^{2}$–$2.61*10^{2}$
p	*nm*	600.00–513.75	795.83–846.83	1056.24–1068.41
φ	*deg*	49.00–80.84	19.37–15.09	0.00–$3.41*10^{-3}$
$l/(\lambda/4)$	*a.u.*	0.57–0.72	0.69–0.77	0.72–0.79
l/w	*a.u.*	1.45–2.04	1.73–2.27	1.88–2.29
$V^{anterior}/V^{exterior}$	*a.u.*	0.15–0.39	1.36–0.92	1.00–1.13
V_{NbN}/V_{Au}	*a.u.*	$3.13*10^{-3}$–$4.53*10^{-3}$	$2.87*10^{-3}$–$3.60*10^{-3}$	$2.49*10^{-3}$–$2.76*10^{-3}$

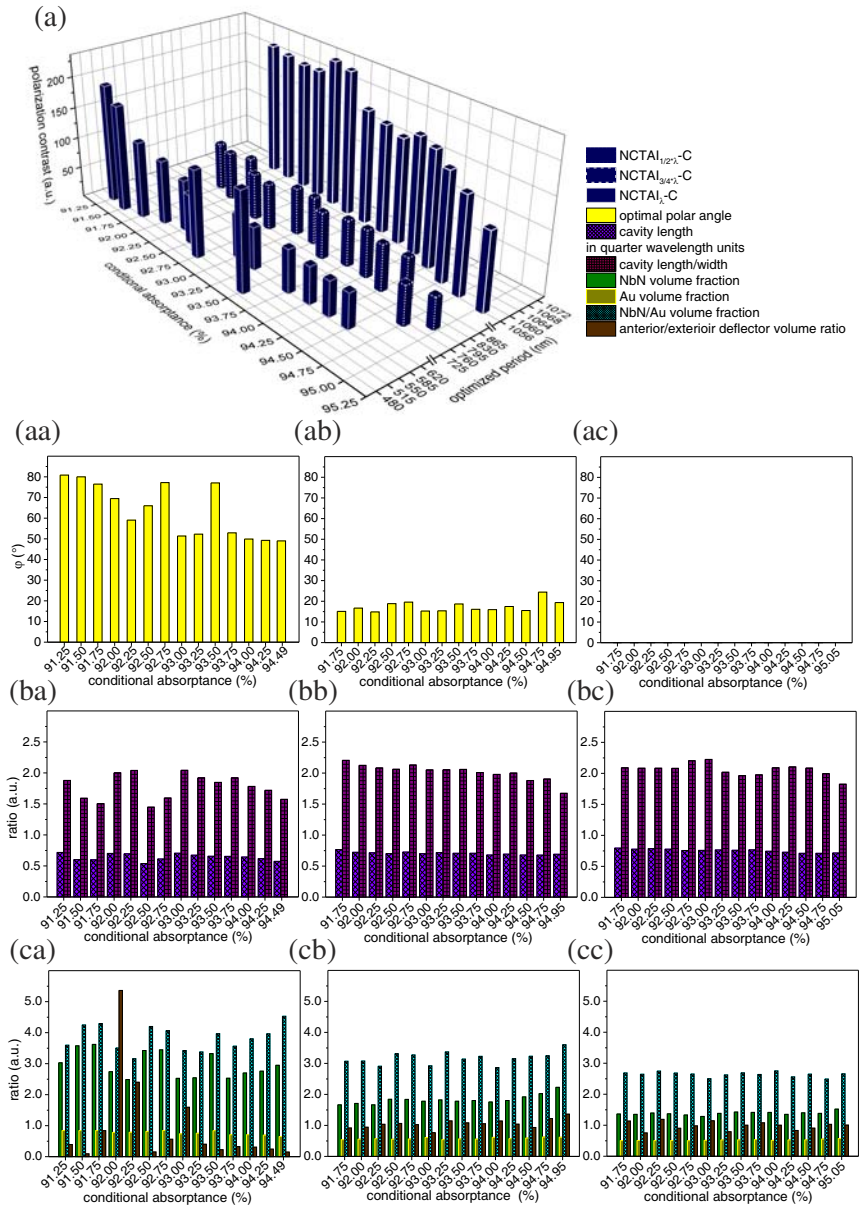

Figure A4. (a) Attained polarization contrast (PC), optimized period (p) and optimal polar angle (φ) as a function of conditional absorptance (CA). Histograms indicating tendencies of (b) cavity length in quarter wavelength units ($l/(\lambda/4)$) and cavity length/width (l/w) ratio qualifying MIM modes squeezing, (c) NbN and Au volume fraction, NbN/Au volume fraction ratio (V_{NbN}/V_{Au}), anterior/exterior deflector volume fraction ratio ($V^{anterior}/V^{exterior}$), all in (a)–(c)/(a) NCTAI$_{1/2*\lambda}$-, (a)–(c)/(b) NCTAI$_{3/4*\lambda}$-, (a)–(c)/(c) NCTAI$_{\lambda}$-C-SNSPD.

modes. Based on these results, the polarization contrast indicates correlation with (extended) cavity length/width, (extended) cavity length in quarter wavelength units and NbN/Au volume fraction ratio parameters. The highest values achievable are on the order of $10^2 - 10^2 - 10^2/10^7 - 10^3 - 10^3/10^9 - 10^8 - 10^{10}/10^2 - 10^1 - 10^2$ in $1/2 * \lambda - 3/4 * \lambda - \lambda$ in NCAI-/NCDAI-/NCDDAI-/NCTAI-C-SNSPDs.

REFERENCES

1. Hadfield, R. H., J. L. Habif, J. Schlafer, R. E. Schwall, and S. W. Nam, "Quantum key distribution at with twin superconducting single-photon detectors," *Applied Physics Letters*, Vol. 89, 241129, 2006.
2. Takesue, H., S. W. Nam, Q. Zhang, R. H. Hadfield, T. Honjo, K. Tamaki, and Y. Yamamoto, "Quantum key distribution over a 40-dB channel loss using superconducting photon-detectors," *Nature Photonics*, Vol. 1, 343, 2007.
3. Honjo, T., S. W. Nam, H. Takesue, Q. Zhang, H. Kamada, Y. Nishida, O. Tadanaga, M. Asobe, B. Baek, R. Hadfield, S. Miki, M. Fujiwara, M. Sasaki, Z. Wang, K. Inoue, and Y. Yamamoto, "Long-distance etanglement-based quantum key distribution over optical fiber," *Optics Express*, Vol. 16, 19118, 2008.
4. Hadfield, R. H., "Single-photon detectors for optical quantum information applications," *Nature Photonics*, Vol. 3, 696, 2009.
5. Eisaman, M. D., J. Fan, A. Migdall, and S. V. Polyakov, "Invited review article: Single-photon sources and detectors," *Review of Scientific Instruments*, Vol. 82, 071101, 2011.
6. Natarajan, C. M., M. G. Tanner, and R. H. Hadfield, "Superconducting nanowire single-photon detectors: Physics and applications," *Superconductor Science and Technology*, Vol. 25, 063001, 2012.
7. Bonneau, D., M. Lobino, P. Jiang, C. M. Natarajan, M. G. Tanner, R. H. Hadfield, S. N. Dorenbos, V. Zwiller, M. G. Thompson, and J. L. Obrien, "Fast path and polarization manipulation of telecom wavelength single photons in lithium niobate waveguide devices," *Physical Review Letters*, Vol. 108, 053601, 2012.
8. Najafi, F., J. Mower, N. C. Harris, F. Bellei, A. Dane, C. Lee, X. Hu, P. Kharel, F. Marsili, S. Assefa, K. K. Berggren, and D. Englund, "On-chip detection of non-classical light by scalable integration of integration of single-photon detectors," *Nature Communications*, Vol. 6, 5873, 2014.
9. Kerman, A. J., E. A. Dauler, W. E. Keicher, J. K. W. Yang, K. K. Berggren, G. Goltsman, and B. Voronov, "Kinetic-inductance-limited reset time of superconducting nanowire photon counters," *Applied Physics Letters*, Vol. 88, 111116, 2006.
10. Rosfjord, K. M., J. K. W. Yang, E. A. Dauler, A. J. Kerman, V. Anant, B. M. Voronov, G. N. Goltsman, and K. K. Berggren, "Nanowire single-photon detector with an integrated optical cavity and anti-reflection coating," *Optics Express*, Vol. 14, 527, 2006.
11. Robinson, B. S., A. J. Kerman, E. A. Dauler, R. J. Barron, D. O. Caplan, M. L. Stevens, J. J. Carney, S. A. Hamilton, J. K. W. Yang, and K. K. Berggren, "781 Mbit/s photon-counting optical communications using a superconducting nanowire detector," *Optics Letters*, Vol. 31/4, 444, 2006.
12. Robinson, B. S., A. J. Kerman, J. K. W. Yang, K. M. Rosfjord, V. Anant, B. Voronov, G. Gol'tsman, and K. K. Berggren, "Multi-element superconducting nanowire single-photon detector," *IEEE Transactions on Applied Superconductivity*, Vol. 17, 279, 2007.
13. Anant, V., A. J. Kerman, E. A. Dauler, J. K. W. Yang, K. M. Rosfjord, and K. K. Berggren, "Optical properties of superconducting nanowire single-photon detectors," *Optics Express*, Vol. 16, 10750, 2008.
14. Dorenbos, S. N., E. M. Reiger, N. Akopian, U. Perinetti, V. Zwiller, T. Zijlstra, and T. M. Klapwijk, "Low noise superconducting single photon detectors on silicon," *Applied Physics Letters*, Vol. 93, 161102, 2008.
15. Divochiy, A., F. Marsili, D. Bitauld, A. Gaggero, R. Leoni, F. Mattioli, A. Korneev, V. Seleznev, N. Kaurova, O. Minaeva, G. Gol'tsman, K. G. Lagoudakis, M. Benkhaoul, F. Lévy, and A. Fiore, "Superconducting nanowire photon-number-resolving detector at telecommunication wavelengths," *Nature Photonics*, Vol. 2, 302, 2008.
16. Dauler, E. A., A. J. Kerman, B. S. Robinson, J. K. W. Yang, B. Voronov, G. Goltsman, S. A. Hamilton, and K. K. Berggren, "Photon-number resolution with sub-30-ps timing using multi-element superconducting nanowire single photon detectors," *Journal of Modern Optics*, Vol. 56,

364, 2009.

17. Marsili, F., D. Bitauld, A. Fiore, A. Gaggero, R. Leoni, F. Mattioli, A. Divochiy, A. Korneev, V. Seleznev, N. Kaurova, O. Minaeva, and G. Goltsman, "Superconducting parallel nanowire detector with photon number resolving functionality," *Journal of Modern Optics*, Vol. 56, 334, 2009.
18. Miki, S., M. Takeda, M. Fujiwara, M. Sasaki, and Z. Wang, "Compactly packaged superconducting nanowire single-photon detector with an optical cavity for multichannel system," *Optics Express*, Vol. 17, 23557, 2009.
19. Baek, B., J. A. Stern, and S. W. Nam, "Superconducting nanowire single-photon detector in an optical cavity for front-side illumination," *Applied Physics Letters*, Vol. 95, 191110, 2009.
20. Bitauld, D., F. Marsili, A. Gaggero, F. Mattioli, R. Leoni, S. J. Nejad, F. Lévy, and A. Fiore, "Nanoscale optical detector with single-photon and multiphoton sensitivity," *Nano Letters*, Vol. 10, 2977, 2010.
21. Gaggero, A., S. J. Nejad, F. Marsili, F. Mattioli, R. Leoni, D. Bitauld, D. Sahin, G. J. Hamhuis, R. Nötzel, R. Sanjines, and A. Fiore, "Nanowire superconducting single-photon detectors and GaAs for integrated quantum photonic applications," *Applied Physics Letters*, Vol. 97, 151108, 2009.
22. Marsili, F., F. Najafi, E. Dauler, F. Bellei, X. Hu, M. Csete, R. J. Molnar, and K. K. Berggren, "Single-photon detectors based on ultra-narrow superconducting nanowires," *Nano Letters*, Vol. 11, 2048, 2011.
23. Csete, M., Á. Sipos, F. Najafi, X. Hu, and K. K. Berggren, "Numerical method to optimize the polar-azimuthal orientation of infrared superconducting nanowire single-photon detectors," *Applied Optics*, Vol. 50/31, 5949, 2011.
24. Hu, X., E. A. Dauler, R. J. Molnar, and K. K. Berggren, "Superconducting nanowire single-photon detectors integrated with optical nano-antennae," *Optics Express*, Vol. 19, 17, 2011.
25. Csete, M., Á. Sipos, F. Najafi, and K. K. Berggren, "Optimized polar-azimuthal orientations for polarized light illumination of different superconducting nanowire single-photon detector designs," *Journal of Nanophotonics*, Vol. 6/1, 063523, 2012.
26. Csete, M., A. Szalai, Á. Sipos, and G. Szabó, "Impact of polar-azimuthal illumination angles on efficiency of nano-cavity-array integrated single-photon detectors," *Optics Express*, Vol. 20/15, 17065, 2012.
27. Akhlaghi, M. K., H. Atikian, A. Eftekharian, M. Loncar, and A. H. Majedi, "Reduced dark counts in optimized geometries for superconducting nanowire single photon detectors," *Optics Express*, Vol. 20/21, 23610, 2012.
28. Verma, V. B., F. Marsili, S. Harrington, A. E. Lita, R. P. Mirin, and S. W. Nam, "A three-dimensional, polarization-insensitive superconducting nanowire avalanche photodetector," *Applied Physics Letters*, Vol. 101, 251114, 2012.
29. Marsili, F., V. B. Verma, J. A. Stern, S. Harrington, A. E. Lita, T. Gerrits, I. Vayshenker, B. Baek, M. D. Shaw, R. P. Mirin, and S. W. Nam, "Detecting single infrared photons with 93% system efficiency," *Nature Photonics*, Vol. 7, 210, 2013.
30. Eftekharian, A., H. Atikian, and A. H. Majedi, "Plasmonic superconducting nanowire single photon detector," *Optics Express*, Vol. 21/3, 3043, 2013.
31. Csete, M., Á. Sipos, A. Szalai, F. Najafi, G. Szabó, and K. K. Berggren, "Improvement of infrared single-photon detectors absorptance by integrated plasmonic structures," *Scientific Reports*, Vol. 3, 2406, 2013.
32. Heath, R. M., M. G. Tanner, T. D. Drysdale, S. Miki, V. Giannini, S. A. Maier, and R. H. Hadfield, "Nano-antenna enhancement for telecom-wavelength superconducting single photon detectors," *Nano Letters*, Vol. 15/2, 819, 2014.

33. Csete, M., G. Szekeres, A. Szenes, A. Szalai, and G. Szabó, "Plasmonic structure integrated single-photon detector configurations to improve absorptance and polarization contrast," *Sensors*, Vol. 15, No. 2, 3513, 2015.
34. Bennett, C. and G. Brassard, "Quantum cryptography: Public key distribution and coin tossing," *Proceedings of IEEE International Conference on Computers, Systems and Signal Processing*, 175–179, 1984.
35. Pryde, G. J., J. L. Obrien, A. G. White, S. D. Bartlett, and T. C. Ralph, "Measuring a photonic qubit without destroying it," *Physical Review Letters*, Vol. 92, 190402, 2004.
36. Knill, E., R. Laflamme, and G. J. Milburn, "A scheme for efficient quantum computation with linear optics," *Nature*, Vol. 409, 46, 2001.
37. Ladd, T. D., F. Jelezko, R. Laflamme, Y. Nakamura, C. Monroe, and J. L. Obrien, "Quantum computers," *Nature*, Vol. 464, 45, 2010.
38. Sánchez-Gil, J. A., "Surface defect scattering of surface plasmon polaritons: Mirrors and light emitters," *Applied Physics Letters*, Vol. 73/24, 3509, 1998.
39. Csendes, T., L. Pál, J. O. H. Sendín, and J. R. Banga, "The GLOBAL optimization method revisited," *Optimization Letters*, Vol. 2, 445, 2008.
40. Bánhelyi, B., T. Csendes, B.M. Garay, and L. Hatvani, "A computer-assisted proof for Sigma_3-chaos in the forced damped pendulum equation," *SIAM Journal on Applied Dinamical Systems*, Vol. 7, 843, 2008.
41. Bánhelyi, B., T. Csendes, T. Krisztin, and A. Neumaier, "Global attractivity of the zero solution for Wright's equation," *SIAM Journal on Applied Dinamical Systems*, Vol. 13, 537, 2014.
42. Al, A., G. Daguanno, N. Mattiucci, and M. J. Bloemer, "Plasmonic Brewster angle: Broadband extraordinary transmission though optical gratings," *Physical Review Letters*, Vol. 106, 123902, 2011.
43. Aközbek, N., N. Mattiucci, D. de Ceglia, R. Trimm, A. Al, G. Daguanno, M. A. Vincenti, M. Scalora, and M. J. Bloemer, "Experimental demonstration of plasmonic Brewster angle extraordinary transmission through extreme subwavelength slit arrays in the microwave," *Physical Review B*, Vol. 85, 205430, 2012.
44. Argyropoulos, C., G. Daguanno, N. Mattiucci, N. Akozbek, M. J. Bloemer, and A. Al, "Matching and funneling light at the plasmonic Brewster angle," *Physical Review B*, Vol. 85, 024304, 2012.
45. Sobnack, M. B., W. C. Tan, N. P. Wanstall, T. W. Preist, and J. R. Sambles, "Stationary surface plasmons on a zero-order metal grating," *Physical Review Letters*, Vol. 80/25, 5667, 1998.
46. Tan, W.-C., T. W. Preist, J. R. Sambles, and N. P. Wanstall, "Flat surface-plasmon-polariton bands and resonant optical absorption on short-pitch metal gratings," *Physical Review B*, Vol. 59/19, 12661, 1999.
47. Hooper, I. R. and J. R. Sambles, "Dispersion of surface plasmon polaritons on short-pitch metal gratings," *Physical Review B*, Vol. 65, 165432, 2002.
48. Hooper, I. R. and J. R. Sambles, "Surface plasmon polaritons on narrow-ridged short-pitch metal gratings," *Physical Review B*, Vol. 66, 205408, 2002.
49. Chen, Y. J., E. S. Koteles, R. J. Seymour, G. J. Sonek, and J. M. Ballantyne, "Surface plasmon on gratings: Coupling in the minigap regions," *Solid State Communications*, Vol. 46/2, 95, 1983.
50. Garcia-Vidal, F. J., J. Sanchez-Dehesa, A. Dechelette, E. Bustarret, T. Lopez-Rios, T. Fournier, and B. Pannetier, "Localized surface plasmons in lamellar metallic gratings," *Journal of Lightwave Technology*, Vol. 17/11, 2191, 1999.
51. Marquier, F., J.- J. Greffet, S. Collin, F. Pardo, and J. L. Pelouard, "Resonant transmission through a metallic film due to coupled modes," *Optics Express*, Vol. 13/1, 70, 2004.
52. de Ceglia, D., M. A. Vincenti, M. Scalora, N. Akozbek, and M. J. Bloemer, "Plasmonic band edge effects on the transmission properties of metal gratings," *AIP Advances*, Vol. 1, 032151, 2011.
53. Collin, S., "Nanostructure arrays in free-space: Optical properties and applications," *Reports on Progress in Physics*, Vol. 77, 126402, 2014.
54. Wood, R. W., "Anomalous diffraction gratings," *Physical Review*, Vol. 15, 928, 1935.

55. Hessel, A. and A. A. Oliner, "A new theory of Wood's anomalies on optical gratings," *Applied Optics*, Vol. 4/10, 1275–1297, 1965.
56. Sarrazin, M., J.-P. Vigneron, and J.-M. Vigoureux, "Role of Wood anomalies in optical properties of thin metallic films with a bidimensional array of subwavelength holes," *Physical Review B*, Vol. 67, 085415, 2003.
57. Philpot, M. R. and J. D. Swalen, "Exciton surface polaritons on organic crystals," *The Journal of Chemical Physics*, Vol. 69, No. 6, 2912, 1978.
58. Welford, K. R., "Surface plasmon-polaritons," *IOP Short Meeting Series*, Vol. 9, 25, 1988.
59. Yang, F., J. R. Sambles, and G. W. Bradberry, "Long-range surface modes supported by thin films," *Physical Review B*, Vol. 44, 5855, 1991.
60. Sarrazin, M. and J.-P. Vigneron, "Light transmission assisted by Brewster-Zennek modes in chromium films carrying a subwavelength hole array," *Physical Review*, Vol. 71, 075404, 2005.
61. Weiner, J., "The physics of light transmission through subwavelength apertures and aperture arrays," *Reports on Progress in Physics*, Vol. 72, 064401, 2009.
62. Torma, P. and W. L. Barnes, "Strong coupling between surface plasmon polaritons and emitters: A review," *Reports on Progress in Physics*, Vol. 78, 013901, 2015.
63. Fan, R.-H., R.-W. Peng, X.-R. Huang, J. Li, Y. Liu, Q. Hu, M. Wang, and X. Zhang, "Transparent metals for ultrabroadband electromagnetic waves," *Advanced Materials*, Vol. 24, 1980, 2012.
64. Sakat, E., G. Vincent, P. Ghenuche, N. Bardou, C. Dupuis, S. Collin, F. Pardo, R. Hadar, and J.-L. Pelouard, "Free-standing guided-mode resonance band-pass filters: From 1D to 2D structures," *Optics Express*, Vol. 20/12, 13082, 2012.
65. Shen, H. and B. Maes, "Enhanced optical transmission through tapered metallic gratings," *Applied Physics Letters*, Vol. 100, 241104, 2012.
66. Barbara, A., P. Quémerais, E. Bustarret, T. López-Rios, and T. Fournier, "Electromagnetic resonances of subwavelength rectangular metallic gratings," *The European Physical Journal D*, Vol. 23, 143, 2003.
67. Tan, W.-C., J. R. Sambles, and T. W. Preist, "Double-period zero-order metal gratings as effective selective absorbers," *Physical Review B*, Vol. 61/19, 13177, 2000.
68. Chan, H. B., Z. Marcet, Kwangje Woo, D. B. Tanner, D. W. Carr, J. E. Bower, R. A. Cirelli, E. Ferry, F. Klemens, J. Miner, C. S. Pai, and J. A. Taylor, "Optical transmission through double-layer metallic subwavelength slit arrays," *Optics Letters*, Vol. 31/4, 516, 2006.
69. Cheng, C., J. Chen, D.-J. Shi, Q.-Y. Wu, F.-F. Ren, J. Xu, Y.-X. Fan, J. Ding, and H.-T. Wang, "Physical mechanism of extraordinary electromagnetic transmission in dual-metallic grating structures," *Physics Review B*, Vol. 78, 075406, 2008.
70. Barbara, A., S. Collin, Ch. Sauvan, J. Le Perchec, C. Maxime, J.-L. Pelouard, and P. Quémerais, "Plasmon dispersion diagram and localization effects in a three-cavity commensurate grating," *Optics Express*, Vol. 18/14, 14913, 2010.
71. Skigin, D. C. and R. A. Depine, "Narrow gaps of transmission through metallic structured gratings with subwavelength slits," *Physics Review E*, Vol. 74, 046606, 2006.
72. Csendes, T., B. M. Garay, and B. Bánhelyi, "A verified optimization technique to locate chaotic regions of a Hénon system," *Journal of Global Optimization* Vol. 35, 145, 2006.